

# Strange Baryon Electromagnetic Form Factors and SU(3) Flavor Symmetry Breaking

Huey-Wen Lin\*

*Thomas Jefferson National Accelerator Facility, Newport News, VA 23606*

Kostas Orginos†

*Department of Physics College of William  
Williamsburg, VA 23187-8795 and*

*Thomas Jefferson National Accelerator Facility, Newport News, VA 23606*

(Dated: Dec. 26, 2008)

We study the nucleon, Sigma and cascade octet baryon electromagnetic form factors and the effects of SU(3) flavor symmetry breaking from 2+1-flavor lattice calculations. We find that electric and magnetic radii are similar; the maximum discrepancy is about 10%. In the pion-mass region we explore, both the quark-component and full-baryon moments have small SU(3) symmetry breaking. We extrapolate the charge radii and the magnetic moments using three-flavor heavy-baryon chiral perturbation theory (HBXPT). The systematic errors due to chiral and continuum extrapolations remain significant, giving rise to charge radii for  $p$  and  $\Sigma^-$  that are 3–4 standard deviations away from the known experimental ones. Within these systematics the predicted  $\Sigma^+$  and  $\Xi^-$  radii are 0.67(5) and 0.306(15) fm<sup>2</sup> respectively. When the next-to-next-to-leading order of HBXPT is included, the extrapolated magnetic moments are less than 3 standard deviations away from PDG values, and the discrepancy is possibly due to remaining chiral and continuum extrapolation errors.

PACS numbers: 11.15.Ha, 12.38.Gc 13.40.Em 13.40.Gp 14.20.Dh

## I. INTRODUCTION

The study of hadron electromagnetic form factors reveals information important to our understanding of hadronic structure. However, experimental measurements on baryons with strange quarks, such as hyperons, are difficult due to their unstable nature. From the theoretical perspective, studies in the nonperturbative regime of quantum chromodynamics (QCD) have been difficult without resorting to model-dependent calculations or making approximations. In lattice QCD, we are able to compute the path integral directly via numerical integration, providing a first-principles calculation of the consequences of QCD. Such study of hadronic form factors together with experiment will serve as valuable theoretical input for understanding hadronic structure.

The nucleon form factors have been calculated on the lattice by many groups, and calculations are still ongoing[1, 2, 3, 4, 5, 6, 7, 8, 9, 10, 11]. However, few have devoted effort to calculating the form factors for other members of the octet. The JLab/Adelaide group[12, 13, 14] performed form factor calculations for the entire octet, and QCDSF collaboration studied the spin structure of the Lambda[15]. Both of these calculations used the quenched approximation, where fermion vacuum-polarization loop contributions are ignored; this introduces an uncontrollable systematic error into their calculations. We recently performed a first lattice calculation of the hyperon axial coupling constants[16] with dynamical fermions, where the SU(3) flavor symmetry breaking was investigated and found to be non-negligible.

The assumption of SU(3) flavor symmetry has been common in studies involving baryonic observables. For example, in the determination of  $V_{us}$  from hyperon decays reported in the PDG[17] (and thus in much experimental work following from it), exact SU(3) is assumed in the  $g_1/f_1$  entry. Symmetry-breaking effects in the axial couplings could therefore impact the world-average  $V_{us}$  value. The SU(3) breaking of baryon masses is relatively small, as in the Gell-Mann–Okubo relation[18, 19] (which has also been studied in a full-QCD lattice calculation[20]) or the decuplet equal-spacing relation. However, this small breaking is in contrast to other quantities with substantial breaking, such as the magnetic moments (as suggested by Coleman and Glashow[21]) or the axial coupling constants[16, 22]. In lattice QCD calculations, we can vary the up/down and strange quark masses to move away from the SU(3)-symmetric point and explicitly observe flavor-breaking effects.

In this work, we concentrate on the electromagnetic properties of octet baryons. This allows us to study SU(3) flavor symmetry within the octet family. The structure of this paper is as follows: In Sec. II, we define the operators used

---

\*Electronic address: hwlin@jlab.org

†Electronic address: kostas@wm.edu

	m010	m020	m030	m040	m050
$N_{\text{prop}}$	612	345	561	320	342
$m_\pi$ (MeV)	354.2(8)	493.6(6)	594.2(8)	685.4(19)	754.3(16)
$M_N$ (GeV)	1.15(3)	1.29(2)	1.366(18)	1.490(14)	1.558(8)
$M_\Sigma$ (GeV)	1.349(19)	1.41(2)	1.448(12)	1.524(14)	1.558(8)
$M_\Xi$ (GeV)	1.438(11)	1.475(16)	1.491(10)	1.546(12)	1.558(8)

TABLE I: Quantities associated with the gauge ensembles used in our calculation

for this calculation and detail how we extract the electromagnetic form factors from lattice calculations. In Sec. III, we discuss the momentum dependence of the form factors and examine the validity of the dipole extrapolations that are commonly used on lattice data. We also extract the electric charge radii, magnetic radii and magnetic moments for the nucleon, Sigma and cascade baryons and discuss the SU(3) flavor-breaking of these quantities. Our conclusions are presented in Sec. IV, and some detailed numbers obtained from this calculation are listed in the appendix.

## II. LATTICE SETUP

For this calculation we use 2+1 flavors of improved staggered fermions (asqtad)[23, 24, 25] for the expensive sea quarks (in configuration ensembles generated by the MILC collaboration[26]), and domain-wall fermions (DWF)[27, 28, 29, 30] for the valence sector. The pion mass ranges from around 350 to 750 MeV in a lattice box of size 2.6 fm. The gauge fields entering the DWF action are HYP[31, 32, 33] smeared to reduce the residual chiral symmetry breaking on the lattice, and the baryon interpolating fields use gauge-invariant Gaussian smeared quark sources to improve the signal. The source-sink separation is fixed at 10 time units. The number of configurations used from each ensemble ranges from 350 to 700; for more details, see Table I (or Table 1 in Ref. [16]).

The interpolating fields we use for the nucleon, Sigma and cascade octet baryons have the general form

$$\chi^B(x) = \epsilon^{abc}[\phi_1^{aT}(x)C\gamma_5\phi_2^b(x)]\phi_1^c(x), \quad (1)$$

where  $C$  is the charge conjugation matrix, and  $\phi_1$  and  $\phi_2$  are any of the quarks  $\{u, d, s\}$ . For example, to create a proton, we want  $\phi_1 = u$  and  $\phi_2 = d$ ; for the  $\Xi^-$ ,  $\phi_1 = s$  and  $\phi_2 = d$ .

The electromagnetic form factors of an octet baryon  $B$  can be written as

$$\langle B(p') | V_\mu(q) | B(p) \rangle(q) = \bar{u}_B(p') \left[ \gamma_\mu F_1(q^2) + \sigma_{\mu\nu} q_\nu \frac{F_2(q^2)}{2M_B} \right] u_B(p) e^{-iq \cdot x} \quad (2)$$

from Lorentz symmetry and vector-current conservation.  $F_1$  and  $F_2$  are the Dirac and Pauli form factors. On the lattice, we calculate the quark-component inserted current,  $V_\mu = \bar{\phi}\gamma_\mu\phi$ , with  $\phi = u, d$  light-quark current and  $\phi = s$  strange-quark vector current. Due to the small chiral symmetry breaking of DWF at finite lattice spacing (on the order of  $(m_{\text{res}}a)^2 \ll 1\%$ [32]), the  $O(a)$  terms for the vector current are highly suppressed. By calculating two-point and three-point correlators on the lattice, we will be able to extract the form factors from Eq. 2.

The octet two-point correlators measured on the lattice are

$$\Gamma_{AC}^{(2),T}(t_i, t; \vec{p}) = \langle \text{tr} (T(\chi_C^B)(\chi_A^B)^\dagger) \rangle = \sum_n \frac{E_n(\vec{p}) + M_n}{2E_n(\vec{p})} Z_{n,A} Z_{n,C} e^{-E_n(\vec{p})(t-t_i)}, \quad (3)$$

where  $A$  and  $C$  indicate the smearing parameters,  $\langle \dots \rangle$  indicates the ensemble average, and  $E_n(\vec{p})$  is  $\sqrt{M_n^2 + p^2}$ .  $\chi^B$  (with  $B \in \{N, \Sigma, \Xi\}$ ) is a baryon interpolating field. The states in Eq. 3 are defined to be normalized as

$$\langle 0 | (\chi_C^B)^\dagger | p, s \rangle_n = Z_{n,C} u_s(\vec{p}), \quad (4)$$

where the spinors satisfy

$$\sum_s u_s(\vec{p}) \bar{u}_s(\vec{p}) = \frac{E(\vec{p})\gamma^t - i\vec{\gamma} \cdot \vec{p} + M_B}{2E(\vec{p})}. \quad (5)$$

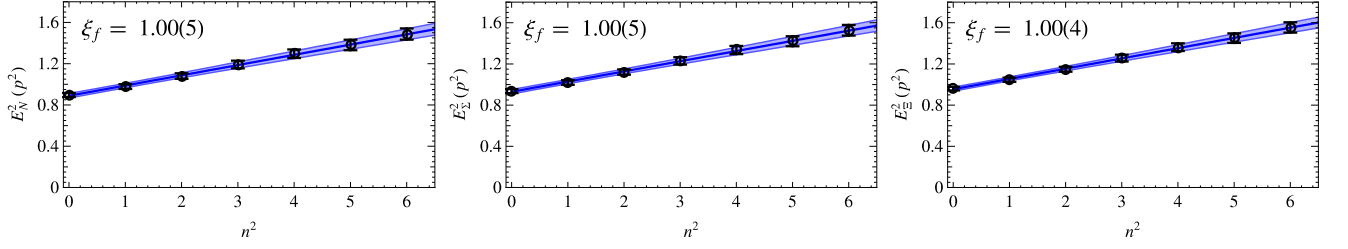


FIG. 1: The dispersion relation of the  $N$  (left),  $\Sigma$  (middle) and  $\Xi$  (right) on ensemble “m040”. The x-axis is in units of  $(\frac{2\pi}{L}a^{-1})^2$ .

The projection used is  $T = \frac{1}{4}(1 + \gamma_4)(1 + i\gamma_5\gamma_3)$ . Since we are only interested in the ground state of each baryon, we tune the smearing parameters and the source-sink separation so that only the ground-state signal remains relevant at larger  $t$ . Therefore,  $n = 0$  in Eq. 3.

The energy of each baryon is measured using a single-exponential fit to the larger-time data. The masses are listed in Table I. We measure baryons with these momenta:

$$\vec{p}_i = \frac{2\pi}{L}a^{-1}\vec{n} \quad (6)$$

$$\vec{n} \in \left\{ \begin{pmatrix} 0 \\ 0 \\ 0 \end{pmatrix}, \begin{pmatrix} 1 \\ 0 \\ 0 \end{pmatrix}, \begin{pmatrix} 1 \\ 1 \\ 0 \end{pmatrix}, \begin{pmatrix} 1 \\ 1 \\ 1 \end{pmatrix}, \begin{pmatrix} 2 \\ 0 \\ 0 \end{pmatrix}, \begin{pmatrix} 2 \\ 1 \\ 0 \end{pmatrix}, \begin{pmatrix} 2 \\ 1 \\ 1 \end{pmatrix} \right\}, \quad (7)$$

and their rotational equivalents. We check the dispersion relation  $E(\vec{p}) = \sqrt{M_n^2 + p^2/\xi_f^2}$  on the ensemble “m040” for each of the octet baryons with our lattice data and find that  $\xi_f$  is consistent with 1; see Figure 1.

Similarly to the two-point function, the lattice three-point function is

$$\begin{aligned} \Gamma_{\mu,AC}^{(3),T}(t_i, t, t_f; \vec{p}_i, \vec{p}_f) &= \langle \text{tr} (T(\chi_C^B)V_\mu(\chi_A^B)^\dagger) \rangle = \sum_n \sum_{n'} \frac{Z_{n',A}(\vec{p}_f)Z_{n,C}(\vec{p}_i)}{Z_V} \\ &\times e^{-(t_f-t)E_n'(\vec{p}_f)} e^{-(t-t_i)E_n(\vec{p}_i)} \times \langle B|V_\mu|B' \rangle, \end{aligned} \quad (8)$$

where  $n$  and  $n'$  index energy states and  $Z_V$  is the vector current renormalization constant, which we will set to its nonperturbative value[32]. Again, we are only interested in the ground state of each baryon, so  $n = n' = 0$  in Eqs. 3 and 8.

If we denote smearing parameters as  $A, C, \dots, I$ , we have the freedom to construct a ratio of three- and two-point functions:

$$\begin{aligned} R_{V_\mu} &= \frac{Z_V \Gamma_{\mu,AI}^{(3),T}(t_i, t, t_f; \vec{p}_i, \vec{p}_f)}{\Gamma_{IC}^{(2),T}(t_i, t_f; \vec{p}_f)} \sqrt{\frac{\Gamma_{DE}^{(2),T}(t, t_f; \vec{p}_i)}{\Gamma_{FH}^{(2),T}(t, t_f; \vec{p}_f)}} \\ &\times \sqrt{\frac{\Gamma_{CC}^{(2),T}(t_i, t; \vec{p}_f)}{\Gamma_{AA}^{(2),T}(t_i, t; \vec{p}_i)}} \sqrt{\frac{\Gamma_{FH}^{(2),T}(t_i, t_f; \vec{p}_f)}{\Gamma_{DE}^{(2),T}(t_i, t_f; \vec{p}_i)}}, \end{aligned} \quad (9)$$

where all the  $Z(\vec{p})$  factors are exactly canceled, as well as the remaining time dependence. In this work, we choose  $D = F = P$ , where  $P$  denotes a point source and choose the rest of the smearing parameters to be  $G$ , denoting Gaussian smearing. Thus,

$$\begin{aligned} R_{V_\mu} &= \frac{Z_V \Gamma_{\mu,GG}^{(3),T}(t_i, t, t_f; \vec{p}_i, \vec{p}_f)}{\Gamma_{GG}^{(2),T}(t_i, t_f; \vec{p}_f)} \sqrt{\frac{\Gamma_{PG}^{(2),T}(t, t_f; \vec{p}_i)}{\Gamma_{PG}^{(2),T}(t, t_f; \vec{p}_f)}} \\ &\times \sqrt{\frac{\Gamma_{GG}^{(2),T}(t_i, t; \vec{p}_f)}{\Gamma_{GG}^{(2),T}(t_i, t; \vec{p}_i)}} \sqrt{\frac{\Gamma_{PG}^{(2),T}(t_i, t_f; \vec{p}_f)}{\Gamma_{PG}^{(2),T}(t_i, t_f; \vec{p}_i)}}, \end{aligned} \quad (10)$$

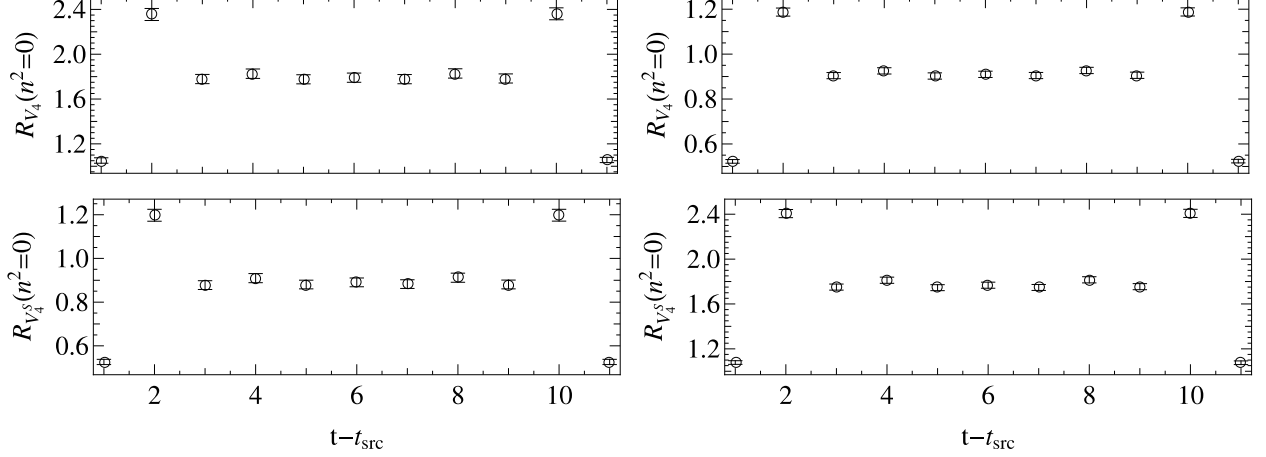


FIG. 2:  $R_{V_\mu}$  from Eq. 10 for  $\langle \Sigma | \bar{\phi} \gamma_4 \phi | \Sigma \rangle$  (left) and  $\langle \Xi | \bar{\phi} \gamma_4 \phi | \Xi \rangle$  (right) with  $\phi = u/d$  (upper panels) and  $\phi = s$  (lower panels) for our lightest-pion ensemble.

Figure 2 shows data from our lightest-pion ensemble for the  $\Sigma$  and  $\Xi$  (with at-rest initial and final baryon states) for the strange- and light-quark vector currents. After a few early time slices, the excited states start to die out and leave the data relatively time-independent.

Throughout this work, we fix the sink momentum to  $\vec{p}_f = (0, 0, 0)$  and vary the initial momentum amongst the list in Eq. 6. The form factors  $F_{1,2}$  in Eq. 2 are connected to  $R_{V_\mu}$  (Eq. 9) through

$$\begin{pmatrix} R_{V_1} \\ R_{V_2} \\ R_{V_3} \\ R_{V_4} \end{pmatrix} = \begin{pmatrix} \frac{2M_B p_y - 2iM_B p_x}{2\sqrt{2}M_B \sqrt{E(M_B, \vec{p}_i)} \sqrt{M_B + E(M_B, \vec{p}_i)}} & \frac{-iM_B p_x + iE(M_B, \vec{p}_i)p_x + 2M_B p_y}{2\sqrt{2}M_B \sqrt{E(M_B, \vec{p}_i)} \sqrt{M_B + E(M_B, \vec{p}_i)}} \\ \frac{-2M_B p_x - 2iM_B p_y}{2\sqrt{2}M_B \sqrt{E(M_B, \vec{p}_i)} \sqrt{M_B + E(M_B, \vec{p}_i)}} & \frac{-2M_B p_x - iM_B p_y + ip_y E(M_B, \vec{p}_i)}{2\sqrt{2}M_B \sqrt{E(M_B, \vec{p}_i)} \sqrt{M_B + E(M_B, \vec{p}_i)}} \\ \frac{ip_z}{\sqrt{2} \sqrt{E(M_B, \vec{p}_i)} \sqrt{M_B + E(M_B, \vec{p}_i)}} & \frac{ip_z (M_B - E(M_B, \vec{p}_i))}{2\sqrt{2}M_B \sqrt{E(M_B, \vec{p}_i)} \sqrt{M_B + E(M_B, \vec{p}_i)}} \\ \frac{\sqrt{M_B + E(M_B, \vec{p}_i)}}{\sqrt{2} \sqrt{E(M_B, \vec{p}_i)}} & \frac{(M_B - E(M_B, \vec{p}_i)) \sqrt{M_B + E(M_B, \vec{p}_i)}}{2\sqrt{2}M_B \sqrt{E(M_B, \vec{p}_i)}} \end{pmatrix} \cdot \begin{pmatrix} F_1 \\ F_2 \end{pmatrix}. \quad (11)$$

We solve for  $F_{1,2}$  using singular value decomposition (SVD) at each time slice from source to sink with data from all momenta with the same  $q^2$  and all  $\mu$ . (Tables VII–XVIII in the appendix summarize all the results.) For example, Figure 3 shows the light vector current inserted  $\Sigma$  and  $\Xi$  form factor data obtained from Eq. 11. The final form factors are obtained from a fit to the plateau.

Another common set of form factor definitions, widely used in experiments, are the Sachs form factors; these can be related to the Dirac and Pauli form factors through

$$G_E(q^2) = F_1(q^2) - \frac{q^2}{4M_B^2} F_2(q^2) \quad (12)$$

$$G_M(q^2) = F_1(q^2) + F_2(q^2). \quad (13)$$

In this work, we only calculate the “connected” diagram, which means the inserted quark current is contracted with the valence quarks in the baryon interpolating fields.

On the lattice, we calculate the matrix element  $\langle B | V^\phi | B \rangle$  with  $V^\phi = \bar{\phi} \gamma_\mu \phi$ . Using SU(2) isospin symmetry, we can connect the proton and neutron matrix elements via

$$u^p \equiv \langle p | V^u | p \rangle = \langle n | V^d | n \rangle \quad (14)$$

$$d^p \equiv \langle p | V^d | p \rangle = \langle n | V^u | n \rangle. \quad (15)$$

Therefore, the proton and neutron form factors are

$$G_{E,M}^p = \frac{2}{3}(G_{E,M})_{u^p} - \frac{1}{3}(G_{E,M})_{d^p} \quad (16)$$

$$G_{E,M}^n = -\frac{1}{3}(G_{E,M})_{u^p} + \frac{2}{3}(G_{E,M})_{d^p}, \quad (17)$$

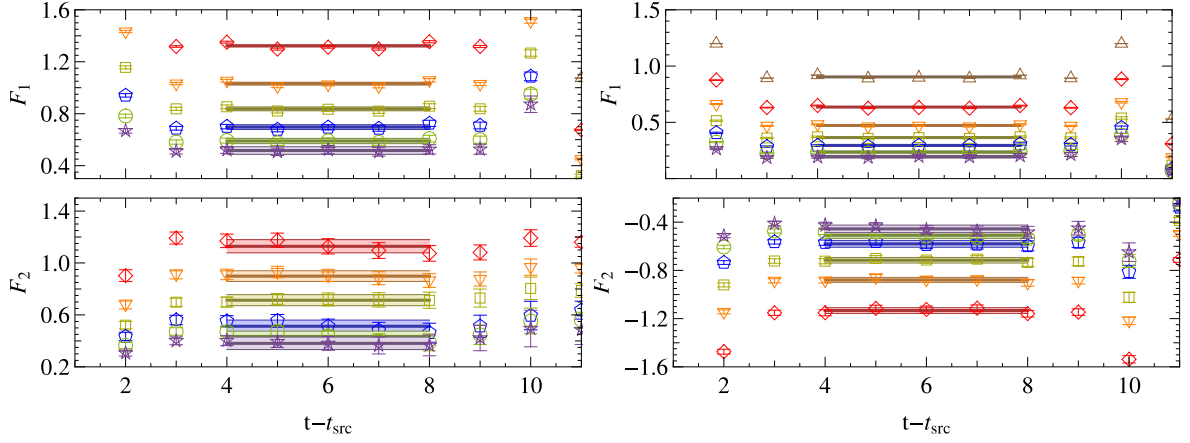


FIG. 3: The light-quark vector current inserted  $\Sigma$  (left) and  $\Xi$  (right) form factor  $F_{1,2}$  for all momenta  $\vec{q}$  at  $m_\pi \approx 600$  MeV. Different symbols represent different transfer momenta: triangles ( $n^2 = 0$ ), diamonds ( $n^2 = 1$ ), reverse triangles ( $n^2 = 2$ ), squares ( $n^2 = 3$ ), pentagons ( $n^2 = 4$ ), circles ( $n^2 = 5$ ), stars ( $n^2 = 6$ ).

where  $(G_{E,M})_{u^p}$  are the Sachs form factors obtained from the  $\langle p|V^u|p\rangle$  matrix element. In the case of the hyperons  $\Sigma$  and  $\Xi$ ,

$$l^\Sigma \equiv \langle \Sigma^+ | V^u | \Sigma^+ \rangle = \langle \Sigma^- | V^d | \Sigma^- \rangle \quad (18)$$

$$s^\Sigma \equiv \langle \Sigma^+ | V^s | \Sigma^+ \rangle = \langle \Sigma^- | V^s | \Sigma^- \rangle \quad (19)$$

$$l^\Xi \equiv \langle \Xi^0 | V^u | \Xi^0 \rangle = \langle \Xi^- | V^d | \Xi^- \rangle \quad (20)$$

$$s^\Xi \equiv \langle \Xi^0 | V^s | \Xi^0 \rangle = \langle \Xi^- | V^s | \Xi^- \rangle. \quad (21)$$

Similarly, for  $\Sigma$  and  $\Xi$  baryons

$$G_{E,M}^{\Sigma^+} = \frac{2}{3}(G_{E,M})_{l^\Sigma} - \frac{1}{3}(G_{E,M})_{s^\Sigma} \quad (22)$$

$$G_{E,M}^{\Sigma^-} = -\frac{1}{3}(G_{E,M})_{l^\Sigma} - \frac{1}{3}(G_{E,M})_{s^\Sigma} \quad (23)$$

$$G_{E,M}^{\Xi^-} = -\frac{1}{3}(G_{E,M})_{l^\Xi} - \frac{1}{3}(G_{E,M})_{s^\Xi} \quad (24)$$

$$G_{E,M}^{\Xi^0} = \frac{2}{3}(G_{E,M})_{l^\Xi} - \frac{1}{3}(G_{E,M})_{s^\Xi}. \quad (25)$$

Figure 4 shows examples of the plateaus for the each of the transfer momenta obtained with Sachs form factors at  $m_\pi \approx 600$  MeV for  $\Sigma^+$  and  $\Xi^-$ . (Tables XIX–XXX in the appendix summarize all the results.)

The magnetic form factors are naturally calculated in units of  $\frac{e}{2M_B}$ , where  $M_B$  is the baryon mass calculated in its corresponding pion sea. In experiment, the nuclear magneton  $\frac{e}{2M_N}$  is generally used in describing the magnetic moments for all baryons. Therefore, to compare with experimental values, we need a conversion factor of  $\frac{M_N}{M_B}$  multiplying our magnetic form factors and moments.

### III. NUMERICAL RESULTS

In this section, we first discuss the behavior of the form factors as functions of momentum transfer squared and compare our data with experimental expectations. Furthermore, we explore the conventional dipole extrapolation used on the form factors and determine that the dipole fit could fail for certain quantities. Later in this section, we discuss the transverse structure of the baryon by studying the charge and magnetic radii, the magnetic moments and the SU(3) flavor symmetry breaking in these quantities.

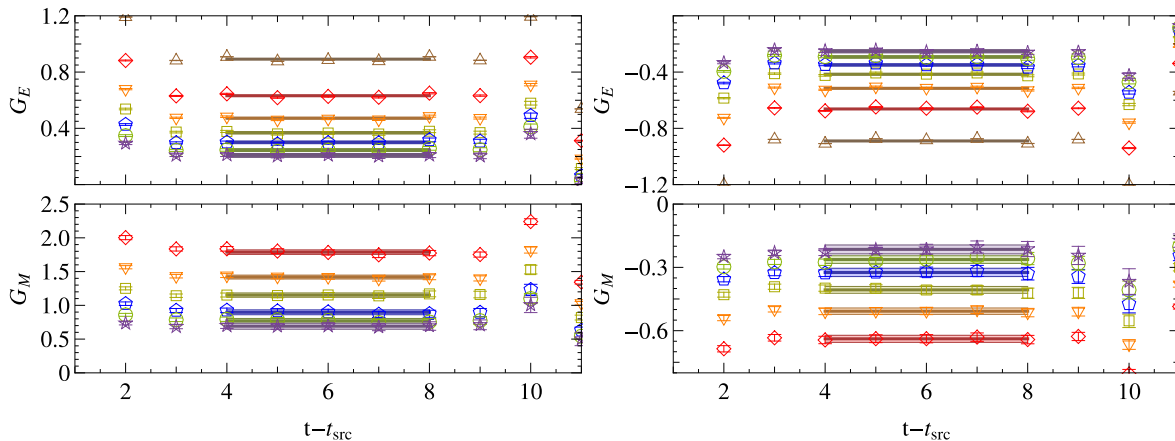


FIG. 4: The  $\Sigma^+$  (left) and  $\Xi^-$  (right) form factors  $G_{E,M}$  for all momentum-transfer dependence at  $m_\pi \approx 600$  MeV. Symbols are the same as Figure 3. Note that  $G_M^B$  here are in units of the natural magneton  $\frac{e}{2M_B}$ , where the  $M_B$  is the baryon mass on the 600-MeV pion sea.

### A. Momentum Dependence of Form Factors

Studying the momentum-transfer ( $Q^2$ ) dependence of the elastic electromagnetic form factors is important in understanding the structure of hadrons at different scales. There have been many experimental studies of these form factors on the nucleon. A recent such experiment, the Jefferson Lab double-polarization experiment (with both a polarized target and longitudinally polarized beam) revealed a non-trivial momentum dependence for the ratio  $G_E^p/G_M^p$ . This contradicts results from the Rosenbluth separation method, which suggested  $\mu_p G_E^p/G_M^p \approx 1$ . The contradiction has been attributed to systematic errors due to two-photon exchange that contaminate the Rosenbluth separation method more than the double-polarization. (For details and further references, see the recent review articles, Refs. [34, 35, 36].) Lattice calculations can make valuable contributions to the study of nucleon form factors, since they allow access to both the pion-mass and momentum dependence of such form factors. In addition, lattice calculations can report individual quark contributions to the baryon form factors. Furthermore, by varying the light-quark masses we can study SU(3) flavor symmetry breaking effects in octet baryons.

The upper-left panels in Figures 5, 6 and 7 show the ratios  $\mu_B G_E^B/G_M^B$ , where  $\mu_B$  is the magnetic moment on the lattice taken from Sec. IIID ( $B$  stands for  $p$ ,  $\Sigma^+$  and  $\Xi^-$  respectively). The straight line on each plot is located at 1, the expected value for the nucleon. The lower-left panels show  $G_E^B$ ; in each, the  $Q^2 = 0$  points are in good consistency with 1. The right-column plots show the magnetic form factors divided by their magnetic moments,  $G_M^B/\mu_B$ .

First, we focus on the nucleon system, which has been widely studied by experiments and lattice calculations.<sup>1</sup> In both  $\mu_p G_E^p/G_M^p$  and  $G_E^p$ , there is a decreasing trend as  $Q^2$  increases. The pion-mass dependence is rather mild in the case of  $\mu_p G_E^p/G_M^p$ . The slope of  $\mu_p G_E^p/G_M^p$  is roughly consistent with those measured in double-polarization experiments, around  $-0.14$ . (For example, see the summary plots in Figure 17 of Ref. [35].) The dashed lines in these plots are the fitted forms of Ref. [34] for the proton and Ref. [37] for the neutron; for this ratio, our points are distributed around the lines, showing there is consistency with the experimental values.  $G_E^p, /G_M^p/\mu_p$  and  $/G_M^p/\mu_n$  shows distinguishable but small pion-mass dependence. As the pion mass decreases, our data appears to trend towards the dashed lines which represent fits to the experimental data.

The hyperon  $\Sigma$  and  $\Xi$  form factors are more poorly known compared with the nucleon case. Similar to the ratio of its SU(3) flavor partner, the ratios  $\mu_{\Sigma^+} G_E^{\Sigma^+}/G_M^{\Sigma^+}$  and  $\mu_{\Xi^-} G_E^{\Xi^-}/G_M^{\Xi^-}$  are around 1 within our  $Q^2$  range, and there is mild pion-mass dependence in our study. Most of the  $\mu_{\Sigma^+} G_E^{\Sigma^+}/G_M^{\Sigma^+}$  values are slightly below experimental proton fitted line, while the  $\mu_{\Xi^-} G_E^{\Xi^-}/G_M^{\Xi^-}$  points are distributed around the line, except for those from 685-MeV pion mass. Since the effect of replacing the up/down quark in the proton is likely suppressed in the ratios of the individual form

<sup>1</sup> Here we only use a subset of the nucleon data available for these ensembles: those which overlap with the hyperon measurements for the Sigma and cascade baryons. The Lattice Hadron Physics Collaboration (LHPC) published a paper on generalized parton distributions (GPDs), which covers slightly more configurations[5], and they will publish an analysis using different source-sink separations and higher statistics in the near future.

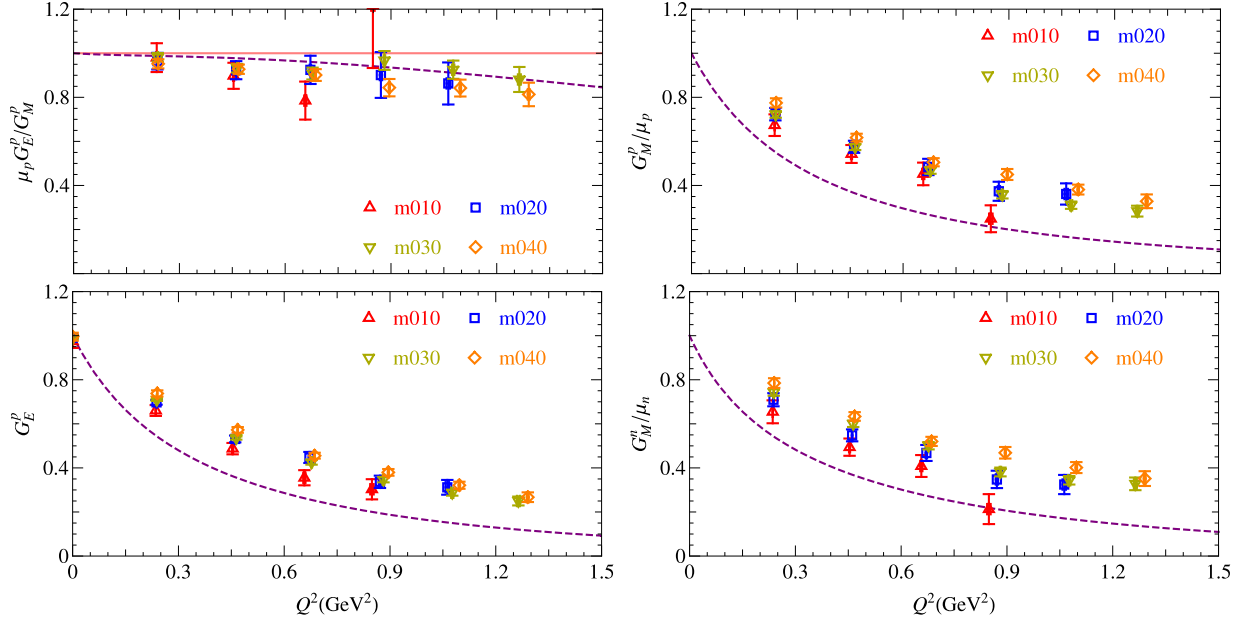


FIG. 5: Nucleon form factors. Left: The ratios  $\mu_p G_E^p / G_M^p$  (top) and  $G_E^p$  (bottom). Right: The magnetic form factor for the proton and neutron divided by their magnetic moments. Different symbols represent different pion-mass ensembles: triangles (m010), squares (m020), reverse triangles (m030) and diamonds (m040). The dashed lines are plotted using experimental form-factor fit parameters[34, 37].

factors, it is not surprising to find that these hyperon form factor ratios are not far from experimental proton line.

$G_E^{\Sigma^+}$ ,  $G_M^{\Sigma^+} / \mu_{\Sigma^+}$  and  $G_M^{\Sigma^-} / \mu_{\Sigma^-}$  have mild discrepancies from nucleon case. The single replacement of a light quark in the nucleon to a strange in the  $\Sigma$  baryon has a mild change on the  $Q^2$  dependence of the form factors. The cascade form factors ( $|G_E^{\Xi^-}|$ ,  $G_M^{\Xi^-} / \mu_{\Xi^+}$  and  $G_M^{\Xi^0} / \mu_{\Xi^0}$ ) are larger than the nucleon case, more dramatically for the lightest quark. The pion-mass dependence is small since the dominant quark flavor (strange) is less sensitive to changes of the up/down masses in the sea and valence sectors. Overall, the hyperon form factors are slightly larger than the nucleon ones, up to 15% in certain cascade channels.

## B. Validity of the Dipole Extrapolation

A widely adopted momentum extrapolation in lattice calculations for electromagnetic form factors is the dipole form

$$\mathcal{F}(Q^2) = \frac{\mathcal{F}(0)}{\left(1 + \frac{Q^2}{M_D^2}\right)^2}, \quad (26)$$

where  $M_D$  is the dipole mass. To demonstrate how well dipole form works for Dirac and Pauli form factors, we can look at

$$r' = \frac{12}{Q^2} \left( \sqrt{\frac{\mathcal{F}(0)}{\mathcal{F}(Q^2)}} - 1 \right). \quad (27)$$

If the dipole form describes the momentum dependence of the form factor, there will be no momentum dependence in  $r'$ .

We first concentrate on the case of Dirac form factors, where  $\mathcal{F}(0) = F_1(0)$  is calculated directly on the lattice (unlike  $F_2(0)$ , which would require extrapolation). Figure 8 shows the results from our  $N$ ,  $\Sigma$  and  $\Xi$  baryons for each inserted quark current. We see almost no momentum dependence of  $r'$  for all of the six matrix elements in Figure 8. This is an indication that the dipole-form is a good description of the data. There are a few cases, such as the “m020” set that seem to deviate from the dipole form at large  $Q^2$ , but a dipole fit still goes through most of the

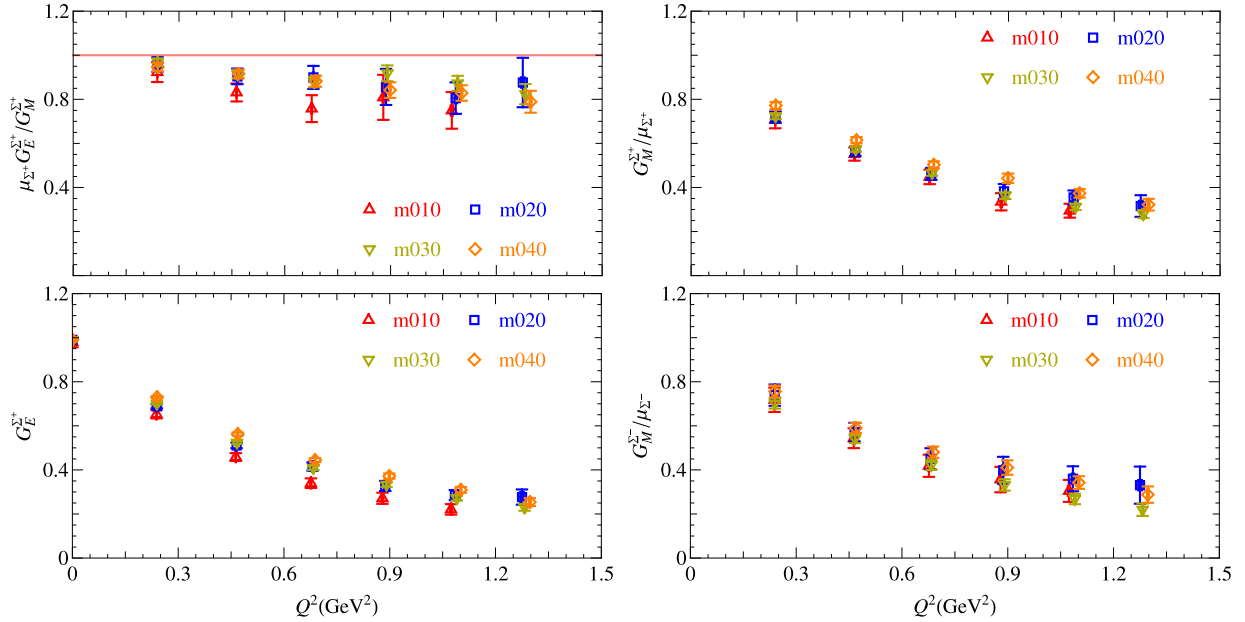


FIG. 6: Sigma form factors. Left: The ratios  $\mu_{\Sigma^+} G_E^{\Sigma^+} / G_M^{\Sigma^+}$  (top) and  $G_E^{\Sigma^+}$  (bottom). Right: The magnetic form factors for the  $\Sigma^+$  and  $\Sigma^-$  divided by their magnetic moments. Symbols are the same as Figure 5.

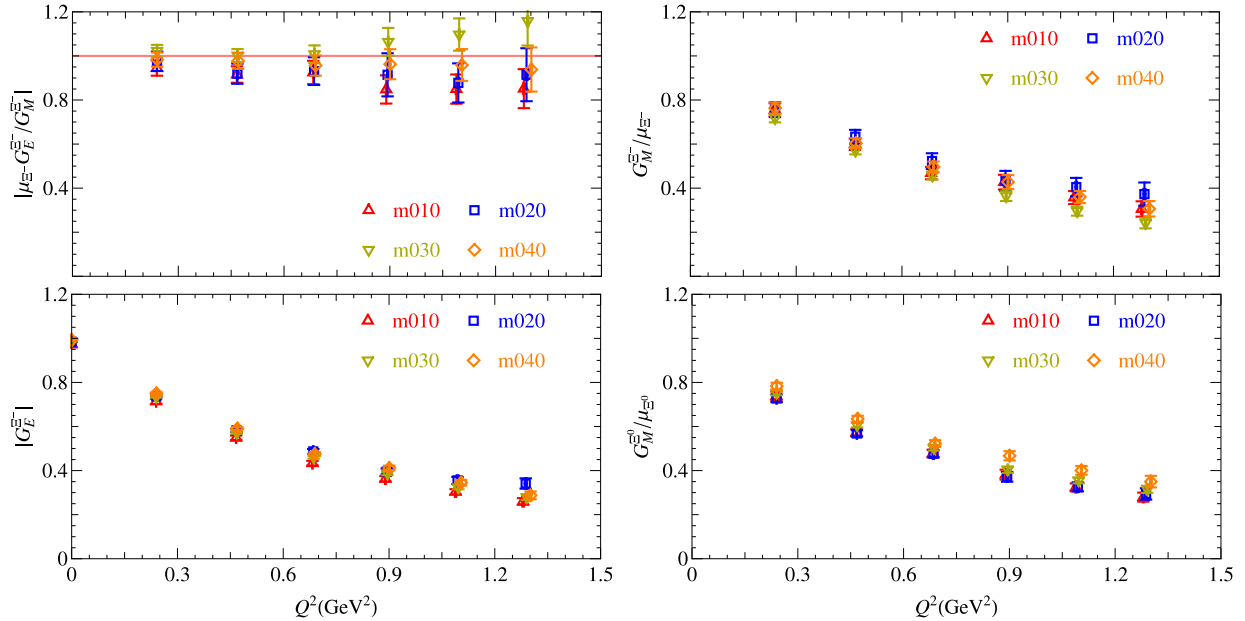


FIG. 7: Cascade form factors. Left: The ratios  $\mu_{\Xi^-} G_E^{\Xi^-} / G_M^{\Xi^-}$  (top) and  $G_E^{\Xi^-}$  (bottom). Right: The magnetic form factors for the  $\Xi^-$  and  $\Xi^0$  divided by their magnetic moments. Symbols are the same as Figure 5.

points. One exception is the light-quark current for the  $\Xi$  baryon matrix element in the “m010” set. In this case the central value of  $r'$  changes about 10% as one goes to large momentum. When quark components are combined to form the full baryon form factors, this discrepancy does not occur, possibly due to cancellation between different quark components. Overall, we observe that  $r'$  for all baryons and most of the quark contributions within the baryons is in good agreement with a constant with respect to  $Q^2$ . In the  $F_2$  case, where  $F_2(0)$  is an unknown constant depending on the matrix element, we find that the dipole description is also reasonable for both quark components and baryons. It is easy to extend Eq. 27 to the electric form factor  $G_E$ , and the results are shown in Figure 9. As before, the largest discrepancy from the dipole description occurs for most of the “m020” set’s quark matrix elements. However, in this

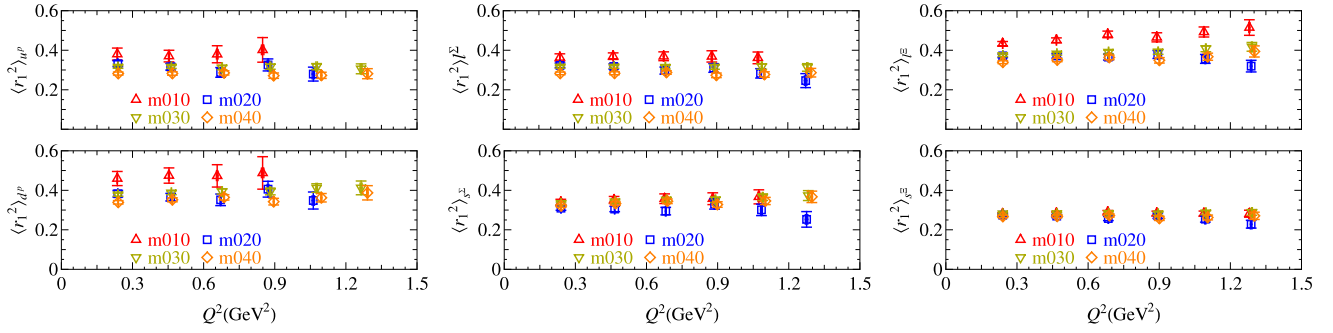


FIG. 8: Dirac mean-squared radii (in units of  $\text{fm}^2$ ) as defined in Eq. 27 as a functions of  $Q^2$  (in units of  $\text{GeV}^2$ ) for  $N$  (left),  $\Sigma$  (middle) and  $\Xi$  (right) for each  $V^\phi$

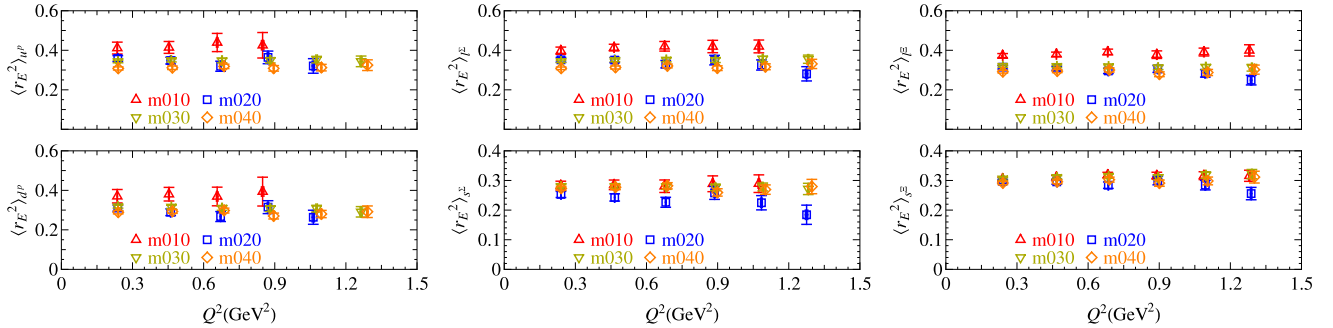


FIG. 9: Electric mean-squared radii (in units of  $\text{fm}^2$ ) as a functions of  $Q^2$  (in units of  $\text{GeV}^2$ ) for  $N$  (left),  $\Sigma$  (middle) and  $\Xi$  (right) for each  $V^\phi$

case the dipole form seems that it does not describe the data well. Although for  $G_M$  no such discrepancy is observed, we need to look for alternative forms to fit the data.

One simple extension is

$$G_E = \frac{1}{(1 + Q^2/M_e^2)^p} \quad (28)$$

with  $p = 1, 2, 3, 4$  for monopole, dipole, tripole and quadrupole. We are also inspired by fit forms used in Refs. [34, 37] to describe the experimental data:

$$G(Q^2) = \frac{\sum_{k=0}^n a_k \tau^k}{1 + \sum_{k=1}^{n+2} b_k \tau^k} \quad (29)$$

with  $\tau = \frac{Q^2}{4M^2}$ . Unfortunately, we do not have comparable amounts of data (and as wide range of  $Q^2$ ) as experiment to adopt the same number of parameters for the fit. Therefore, we constrain the fit form to go asymptotically to  $1/Q^4$  at large  $Q^2$  and to have  $G_E(Q^2 = 0) = 1$ :

$$G_E = \frac{AQ^2 + 1}{CQ^2 + 1} \frac{1}{(1 + Q^2/M_d^2)^2}, \quad (30)$$

where  $C$  may be constrained to be positive to avoid putting unphysical poles within our  $Q^2$  range. The choice of  $C = 0$  and  $A$  free we call “dipoleV0”;  $C > 0$  and  $A$  free we call “dipoleV1”; and  $C > 0$  and  $A > 0$ , “dipoleV2”. Since the  $\Xi$  matrix elements deviate from the dipole form the most, we chose them to test for these new fit forms. Table II summarizes the fitted  $\chi^2/\text{dof}$  using these different fit forms and the electric mean-squared charge radii obtained from the fits to the light-quark component of the cascade. We find that using “dipoleV1”, we get a coefficient  $C$  that is consistent with zero; the fitted results are very close to the result from “dipoleV0”. The extracted electric mean-squared charge radii obtained from dipole fit forms are as much as 8% larger than those from the fit form that describes the lattice data well. Therefore, for the rest of this paper, we will use “dipoleV0” to fit quark-component  $G_E$  and use the standard dipole for all the other form factors.

$m_\pi^2(\text{GeV}^2)$	monopole	dipole	tripole	quadrupole	dipoleV0	dipoleV1	dipoleV2
0.1256(15)	0.462(16)	0.381(12)	0.357(11)	0.345(10)	0.370(10)	0.368(11)	0.381(12)
	[7.64]	[0.31]	[0.28]	[0.9]	[0.12]	[0.15]	[0.47]
0.246(2)	0.353(14)	0.305(11)	0.289(10)	0.282(10)	0.328(10)	0.328(8)	0.305(11)
	[0.87]	[1.17]	[2.63]	[3.7]	[0.43]	[0.54]	[1.75]
0.3493(17)	0.370(9)	0.318(7)	0.301(6)	0.293(6)	0.322(5)	0.314(16)	0.318(7)
	[6.74]	[0.09]	[1.89]	[3.82]	[0.02]	[0.02]	[0.14]
0.463(3)	0.338(11)	0.292(9)	0.278(8)	0.271(8)	0.294(7)	0.27(2)	0.292(9)
	[4.15]	[0.36]	[1.03]	[1.85]	[0.43]	[0.48]	[0.54]

TABLE II: Cascade electric mean-squared charge radii,  $\langle r_E^2 \rangle_{I\Xi}$ , in units of  $\text{fm}^2$  from different fit forms. The square brackets indicate the  $\chi^2/\text{dof}$  for each fit.

### C. Charge Radii

The mean-squared electric charge radii can be extracted from electric form factor  $G_E$  via

$$\langle r_E^2 \rangle = (-6) \frac{d}{dQ^2} \left( \frac{G_E(Q^2)}{G_E(0)} \right) \Big|_{Q^2=0}. \quad (31)$$

Similar definitions can be used to find the Dirac and Pauli radii,  $r_{1,B}$  and  $r_{2,B}$  respectively, where the relations are  $r_{E,B}^2 = r_{1,B}^2 + \frac{3}{2} \frac{\kappa_B}{2m_B^2}$  with  $\kappa_B = F_{2,B}(Q^2 = 0)$ . In Subsec. III B, we discuss an alternative fit form, ‘‘dipoleV0’’, that works better in our kinematic region. Therefore, we will use this form to extract mean-squared electric radii; the numbers are summarized in Table III and Figure 10.

In the left-hand panel of Figure 10, we plot the quark contributions to the nucleon, Sigma and cascade baryons. The upper plot displays the dominant (two-valence) quark contributions in the  $p$ ,  $\Sigma$  and  $\Xi$ , while the lower one shows the single-quark contributions. These charge radii tend to increase in the light sector, while the strange sector is relatively flat as one changes the pion mass. The rightmost points are closest to the SU(3) point, where the quark-contribution differences are the smallest. As one increases the difference in light and strange-quark masses, only the strange-quark contribution in the baryon starts to show differences depending on the baryon species, while the light-quark contribution seems to be independent of its surrounding environment for pion masses as light as 350 MeV. It is expected that the strange contribution displays relatively smaller charge radius, since the strange quark is heavier and thus has shorter Compton wavelength.

We further compare the strange-quark contributions in the  $\Sigma$  and  $\Xi$ , as shown in Figure 11. The strange quark in the cascade has slightly larger contribution to the charge radii than in the Sigma, but overall they agree within  $1.5\sigma$ . This also shows that the quark contribution is not much affected by the environmental baryon, at least down to 350-MeV pion mass.

In the right-hand panel of Figure 10 we plot the electric charge radii with the neutron and  $\Xi^0$  omitted, since they are neutral particles and  $G_{E,\{n,\Xi^0\}}(Q^2) \approx 0$  within our statistical errors. Firstly, we see that there is small SU(3) symmetry breaking between the SU(3) partners,  $p$  and  $\Sigma^+$  (or  $\Sigma^-$  and  $\Xi^-$ ); their charge radii are consistent within statistical errors. A similar observation can also be made for the previous lattice quenched study, Ref. [13]. We observe roughly the same slope for the charge radii of  $p$  and  $\Sigma^{+/-}$  baryons; however, our  $\Xi^-$  has about half the increase with decreasing pion mass; this difference could be caused by the quenched approximation. Overall, the SU(3) symmetry breaking in the charge radii is much smaller than what we observed in our study of the axial coupling constants[16]; this suggests that different physical observables can have substantially different responses to the replacement of one quark by another in a baryon. For charge radii, the effect is negligible.

For the extrapolation of charge radii<sup>2</sup> to physical masses, we adopt continuum three-flavor heavy-baryon chiral

<sup>2</sup> In this work, we use HBXPT to perform the mass extrapolation for charge radii. Other extrapolations, such as Finite-Range Regulation (FRR), are used for octet charge radii on quenched lattice data in Ref. [12], applying corrections to the effective field theory to account for quenching.

perturbation theory (HBXPT)[38, 39, 40, 41, 42]:

$$\langle r_E^2 \rangle = -\frac{6}{(f_\pi^{\text{lat}})^2} c' + \frac{3}{2m_B^2} b' - \frac{1}{16\pi^2 (f_\pi^{\text{lat}})^2} \sum_X [\mathcal{G}(m_X, \delta, f_\pi^{\text{lat}}) + \mathcal{H}(m_X, \delta, f_\pi^{\text{lat}})] \quad (32)$$

$$\mathcal{G}(m, \delta, \mu) = (\gamma_X - 5\beta_X) \ln\left(\frac{m^2}{\mu^2}\right) \quad (33)$$

$$\mathcal{H}(m, \delta, \mu) = 10\beta'_X \mathcal{F}(m, \delta, \mu) \quad (34)$$

$$\mathcal{F}(m, \delta, \mu) = \ln\left(\frac{m^2}{\mu^2}\right) - \frac{\delta}{\sqrt{\delta^2 - m^2}} \ln \frac{\delta - \sqrt{\delta^2 - m^2 + i\epsilon}}{\delta + \sqrt{\delta^2 - m^2 + i\epsilon}}. \quad (35)$$

In the above,  $c' = (Qc_- + \alpha_D c_+)$  and  $b' = (Q\mu_F + \alpha_D \mu_D)$  as in Ref. [41] with coefficients  $Q$  and  $\alpha_D$  listed in Table 1, and  $\gamma_X$  and  $\beta_X^{(j)}$  are given in Tables II–VIII for various baryon flavors. The sum over  $X$  includes all possible meson-loop contributions to the electric charge radii,  $\delta$  is the mass difference between an octet baryon and its decuplet partner, and  $m_B$  is the octet baryon mass; these numbers are taken from LHPC[32]. The octet axial couplings  $D$  and  $F$  are set to 0.715(50) and 0.453(50) respectively from a numerical determination in the same mixed-action calculation[16]; the coupling  $C$  which is related to  $g_{\pi N\Delta}$  is set to be 0 (when ignoring decuplet contributions) or 1.2(2) from an axial  $\Delta - N$  transition form factor calculation[43]. Note that we replace the scale  $\mu$  in the original formulation with  $f_\pi^{\text{lat}}$ [10, 44, 45]. To next-to-leading order in our calculation, such a replacement is consistent with the original formulation.

We reorganize Eq. 32 as follows:

$$\mathcal{I}_{r^2} = 16\pi^2 (f_\pi^{\text{lat}})^2 \langle r_E^2 \rangle - \sum_X [\mathcal{G}(m_X, \delta, f_\pi^{\text{lat}}) + \mathcal{H}(m_X, \delta, f_\pi^{\text{lat}})] \quad (36)$$

$$= 96\pi^2 c' + \left[ 24\pi^2 \left( \frac{f_\pi^{\text{lat}}}{m_B} \right)^2 \right] b'. \quad (37)$$

Such an arrangement converts potential chiral-log terms and a multidimensional parametrization into a simple linear extrapolation. Similar procedures have been adopted by NPLQCD collaboration for  $f_K/f_\pi$  extrapolation[4, 44]. We study the effects of adding decuplet baryons as dynamical degrees of freedom by setting  $C = 0$  and see how they affect our final extrapolation results. Figure 12 shows  $\mathcal{I}_{r^2}$  as functions of  $x = \left[ 24\pi^2 \left( \frac{f_\pi^{\text{lat}}}{m_B} \right)^2 \right]$  for the  $p$ ,  $\Sigma^+$ ,  $\Sigma^-$  and  $\Xi^-$  baryons;  $C = 1.2(2)$  and  $C = 0$  are shown as black and gray points respectively. We find that our lattice data fall onto a straight line for both  $C$ , as Eq. 37 predicts; thus, the extrapolation is straightforward. We summarize the extrapolations in Table III and display fits in Figure 12.

Using the data from all ensembles we find consistent (within one standard deviation) results for both  $C = 0$  and  $C = 1.2(2)$ . This indicates that for our data, the effects of the decuplet intermediate states are relatively mild. The contributions from the  $\mathcal{H}$  function are larger for all channels than those from  $\mathcal{G}$ . We observe that the values of  $\mathcal{I}_{r^2}$  with  $C$  zero and non-zero are very different; however, it turns out that the difference is absorbed into the  $c'$  parameter, while  $b'$  remains consistent in both cases. As shown in Fig. 12, there is only an overall constant shift between the two choices of  $C$ . Thus, we find that there is not much impact on the final extrapolated charge radii from including decuplet-baryon effects.

To better understand the systematic error associated with our extrapolation, we try restricting our fit to the lightest two ensembles, since the convergence of NLO HBXPT formulations could be poor at higher masses. The results are summarized in Table III; they are consistent with the fits using all ensembles. The errorbar of the extrapolated values are larger, which is expected since we have fewer data points with larger statistical errors to constrain the fit. The addition of decuplet degrees of freedom is generally negligible, and we find that HBXPT at NLO has been working well in our extrapolation of charge radii. Comparing to experiment, we get electric mean-squared charge radii for the proton and  $\Sigma^-$  0.54(7) and 0.32(2) fm<sup>2</sup> which are 3.4 and 4.3 $\sigma$  away from the PDG values[17] (0.766(12) and 0.61(16) fm<sup>2</sup> respectively), if all the data are included in the fit. If we concentrate on the results obtained from fits to the lightest two ensembles, the deviation is between 1 and 2 $\sigma$ . These deviations may be caused by lattice artifacts, such as the omission of lattice spacing and volume extrapolation and the higher-order effects from HBXPT. In the case of the proton, it has been observed in previous lattice calculations (for example, Refs. [7, 10, 46]) that the lattice numbers even at 350-MeV pion mass are smaller than experiment. It seems likely that pion-loop contributions are quite large, boosting these values for pion masses smaller than 300 MeV. Resolving this will be a challenge for future lattice calculations.

In addition to the known radii, we can make predictions for electric charge radii of the  $\Sigma^+$  and  $\Xi^-$ : 0.67(5) and 0.306(15) fm<sup>2</sup> respectively. However, judging from our comparison with the known result for  $p$  and  $\Sigma^-$ . Since these

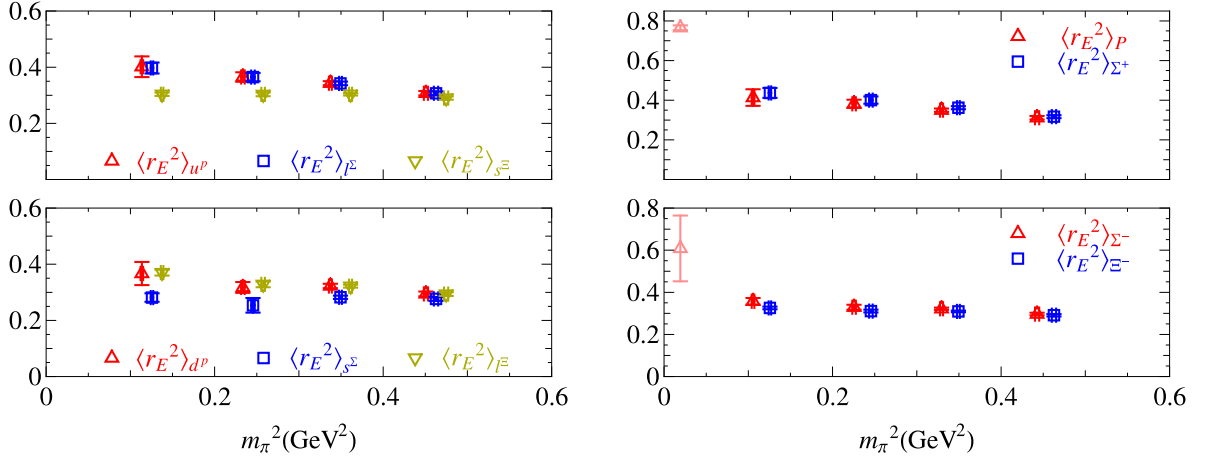


FIG. 10: The electric mean-squared radii in units of  $\text{fm}^2$  as functions of  $m_\pi^2$  (in  $\text{GeV}^2$ ) from each quark contribution (left) and baryon (right). The leftmost triangles in both figures are the extrapolated values at the physical pion mass.

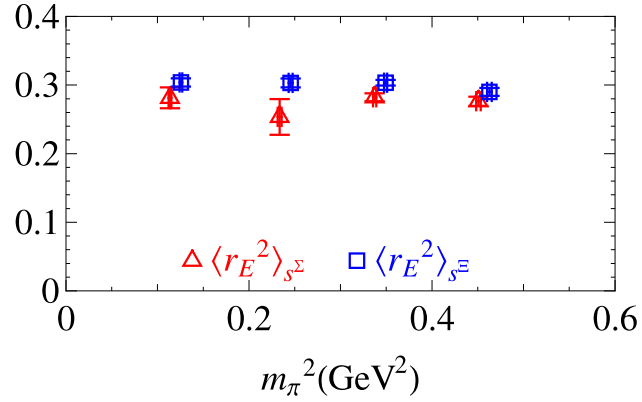


FIG. 11: The strange-quark contribution to the electric mean-squared radii in units of  $\text{fm}^2$  as functions of  $m_\pi^2$  (in  $\text{GeV}^2$ )

quantities should have similar systematics as the ones known experimentally we should add a systematic error that is 2 to 3 times the statistical error.

#### D. Magnetic Moments and Magnetic Radii

Studying the momentum-transfer dependence of magnetic form factors gives us the magnetic moment via

$$\mu_B = G_M^B(Q^2 = 0) \quad (38)$$

with natural units  $\frac{e}{2M_B}$ , where  $M_B$  are the baryon ( $B \in \{N, \Sigma, \Xi\}$ ) masses. To compare among different baryons, we convert these natural units into nuclear magneton units  $\mu_N = \frac{e}{2M_N}$ ; therefore, we convert the magnetic moments with factors of  $\frac{M_N}{M_B}$ . The magnetic radii are also obtained through

$$\langle r_M^2 \rangle = (-6) \frac{d}{dQ^2} \left( \frac{G_M(Q^2)}{G_M(0)} \right) \Big|_{Q^2=0}. \quad (39)$$

The magnetic moment is linked to the Pauli magnetic moment (or anomalous magnetic moment,  $\kappa_B = F_{2,B}(Q^2 = 0)$ ) by  $\mu_B = \kappa_B + e_B$ , where  $e_B$  is the charge of baryon. The magnetic radii are related to the Pauli radii,  $r_{2,B}$  through  $r_{M,B}^2 = r_{2,B}^2 + \frac{3}{2} \frac{\kappa_B}{2M_B^2}$ .

$m_\pi^2(\text{GeV}^2)$	$p$	$\Sigma^+$	$\Sigma^-$	$\Xi^-$
0.1256(15)	0.41(4)	0.44(3)	0.357(16)	0.326(6)
0.246(2)	0.382(21)	0.401(18)	0.329(12)	0.311(7)
0.3493(17)	0.350(8)	0.362(8)	0.322(5)	0.309(4)
0.463(3)	0.312(9)	0.317(8)	0.297(6)	0.291(5)
$C = 0$	0.56(7)[0.19]	0.69(5)[1.09]	0.35(3)[0.06]	0.329(15)[0.72]
$C = 1.2(2)$	0.54(7)[0.21]	0.67(5)[0.86]	0.32(3)[0.07]	0.306(15)[0.31]
$C = 0$ (2pts)	0.59(14)[n/a]	0.70(7)[n/a]	0.34(5)[n/a]	0.34(3)[n/a]
$C = 1.2(2)$ (2pts)	0.55(14)[n/a]	0.67(7)[n/a]	0.31(5)[n/a]	0.31(3)[n/a]
Exp't	0.766(12)	n/a	0.61(16)	n/a

TABLE III: Mean-squared charge radii for octet baryons. The numbers in square brackets indicate the  $\chi^2/\text{dof}$  of the fits.

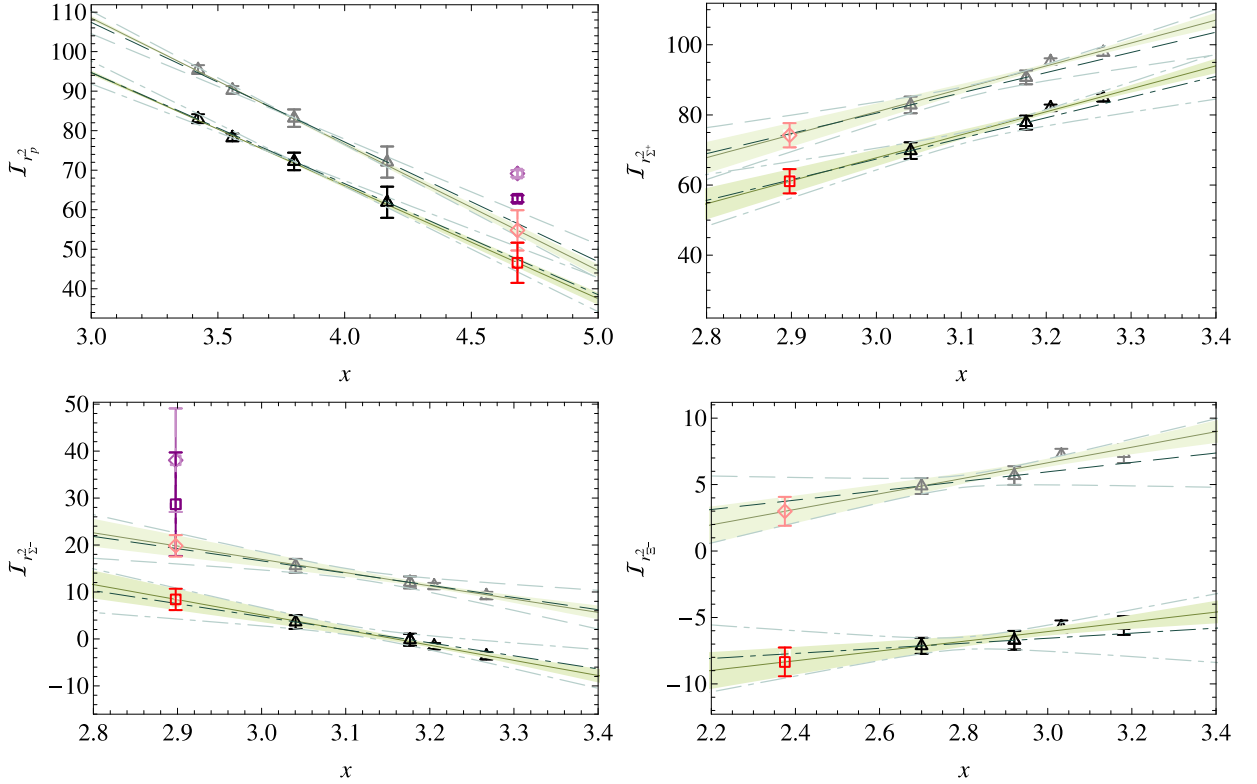


FIG. 12: Chiral extrapolations using  $C = 1.2(2)$  and  $C = 0$  in Eq. 36. The triangles are the lattice data points  $\mathcal{I}_{r,2}$ ; black points indicate  $C = 1.2$  values and the gray are  $C = 0$ . The extrapolation using all ensembles is shown as a band and the red (and pink) symbols indicate the extrapolated value at physical limit. The (dot-)dashed lines show the extrapolations using the lightest two ensembles for  $C = 0$  and  $C = 1.2(2)$  respectively. The purple squares and diamonds are the  $\mathcal{I}_{r,2}$  with experimental values of the charge radii and masses for  $C = 0$  and  $C = 1.2(2)$  respectively.

It is straightforward to extrapolate the magnetic form factor using the dipole form, and the results are summarized in Tables IV and V). If SU(3) symmetry is exact, we expect the octet magnetic moments to obey the Coleman-Glashow relations[21]:

$$\mu_{\Sigma^+} = \mu_p; \mu_{\Xi^0} = \mu_n; \mu_{\Xi^-} = \mu_{\Sigma^-}. \quad (40)$$

In nature, such an SU(3) symmetry approximately holds between the proton and  $\Sigma^+$ , but is broken by more than 50% in the case of  $\{n, \Xi^0\}$  and  $\{\Sigma^-, \Xi^-\}$ . The left panel of Figure 13 shows the magnetic moments of each baryon compared with its SU(3) partner, as paired up in Eq. 40. We find that as seen in experiment, the SU(3) breaking on the magnetic moments are rather small. As we go to larger pion masses (that is, as the light mass goes to the strange

mass), the discrepancy gradually goes to zero as SU(3) is restored. But even at our lightest pion mass, around 350 MeV, the effects of SU(3) symmetry breaking effect can be ignored. In all the baryon magnetic moments calculated in this work, we find only small changes as we decrease the pion mass to around 350 MeV.

The right panel of Figure 13 shows magnetic radii from a dipole fit to the magnetic form factors. Once again, we see small SU(3) flavor breaking even on our lightest pion-mass ensembles. Comparing with Ref. [13], where the quenched approximation is used, we observe that  $\langle r_M^2 \rangle_p \approx \langle r_M^2 \rangle_{\Sigma^+}$ ; however, a larger rate of increase with decreasing pion mass is shown in their data.  $\langle r_M^2 \rangle_n$  becomes larger than  $\langle r_M^2 \rangle_{\Xi^0}$  only at the lightest pion mass. Overall, our data suggests that the magnetic radius's dependence on the quark content is mild and may only start to dominate at very light pion mass, a result which is quite different from quenched calculations.

Alternatively, we can obtain the magnetic moments and radii from polynomial fitting to the ratio of magnetic and electric form factors,  $G_M/G_E$ . From the definition of the electric and magnetic radii, Eqs. 31 and 39, we expect that  $G_E^B/G_M^B \approx \frac{1}{\mu_p} \frac{Q^2}{6} (\langle r_E^B \rangle_p - \langle r_M^2 \rangle_B)$ . From Figures 5, 6 and 7, we expect that ratio to be around 1 with small deviations; thus, we fit  $G_M/G_E \approx A(1 + BQ^2)$  where magnetic moment is  $\mu = AG_E(0)$ , and  $B$  is proportional to  $\langle r_M^2 \rangle - \langle r_E^2 \rangle$ . In the case of  $n$  and  $\Xi^0$ , we use  $G_E^p$  and  $G_E^{\Xi^-}$  in the ratio instead of  $G_E^n$  and  $G_E^{\Xi^0}$ . Table VI summarizes the magnetic moments, which appear consistent with the dipole extrapolation approach. The left panel of Figure 14 shows the magnetic moment (top) and the difference between the electric and magnetic radii for the proton,  $\Sigma^+$  and  $\Xi^-$ . Both results are consistent with what we obtained from the dipole extrapolations. We examine the radii differences from the quark contributions, as shown in the right panel of Figure 14 and observe less than 10% discrepancy. The ratio approach also benefits from cancellation of noise due to the gauge fields, and thus it has smaller statistical error. Therefore, we will concentrate on the results from this approach for the rest of this work.

The HBXPT for octet magnetic moments has been derived in Refs. [40, 47, 48, 49]. The most general form including the dynamical decuplet degrees of freedom is

$$\mu_B = b' + \frac{M_B}{4\pi (f_\pi^{\text{lat}})^2} \sum_X \left\{ \zeta_X M_X + \zeta'_X \frac{C^2}{\pi} \left[ -\mathcal{F}(M_X, \delta, f_\pi^{\text{lat}}) + \frac{5}{3} \right] \right\}, \quad (41)$$

where  $b'$ ,  $\delta$ ,  $m_B$ ,  $X$ ,  $C$  and  $\mathcal{F}$  are defined in Sec. III C, the scale  $\mu$  is replaced by  $f_\pi^{\text{lat}}$ , and  $\zeta_X^{(i)}$  can be found in Tables II–IX of Ref. [49]. As before, we can rewrite Eq. 41 as

$$\mathcal{I}_{\mu_B} = \mu_B - \frac{M_B}{4\pi (f_\pi^{\text{lat}})^2} \sum_X \left\{ \zeta_X M_X + \zeta'_X \frac{C^2}{\pi} \left[ -\mathcal{F}(M_X, \delta, f_\pi^{\text{lat}}) + \frac{5}{3} \right] \right\} \quad (42)$$

$$= b'; \quad (43)$$

therefore, NLO SU(3) HBXPT predicts the lattice data to be flat over the various pion masses. We plot  $\mathcal{I}_{\mu_B}$  from our calculations in Fig. 15 (with decuplet dynamical freedom (black points) and without (gray)) as triangles for the proton and  $\Sigma^-$ . Our data do not show a flat plateau, but instead are linearly dependent on the pion mass.

There are a couple of possibilities which might explain this behavior:

- There might be systematic errors entering our magnetic moments during the extrapolation to zero momentum. However, this can be excluded since we compare both dipole extrapolation of magnetic moments and linear extrapolation to  $Q^2 = 0$  of the ratios  $G_M/G_E$ , finding consistent magnetic moments.
- Or our pion masses may still be too heavy for the NLO formulation to work. We might simply need to go to NNLO to find a better description.

To better extrapolate our data, we examine for the possibility of adding a selection of terms from NNLO HBXPT. Following suggestions in Ref. [50], we expect corrections from terms proportional to  $m_\pi^2$  and  $m_\pi^2 \ln \frac{m_\pi^2}{\mu^2}$  and that there is a parameter which depends on  $\mu$  to absorb the divergence of the second term. Therefore, we propose a modified  $\mathcal{I}_{\mu_B}$ :

$$\mathcal{I}'_{\mu_B} = \mathcal{I}_{\mu_B} - \omega m_\pi^2 \ln \frac{m_\pi^2}{\mu^2} = b' + e' m_\pi^2. \quad (44)$$

However, the coefficient,  $\omega$ , has not yet been calculated. Note that in NLO HBXPT for both charge radii and magnetic moments, there are also log terms when one includes the decuplet degree of freedom. In both cases, we only see an overall constant shift throughout our pion-mass regions which does not affect the charge radii or magnetic moments at the physical point. Therefore, we will neglect such contribution and extrapolate  $\mathcal{I}_{\mu_B}$  in terms of  $m_\pi^2$ .

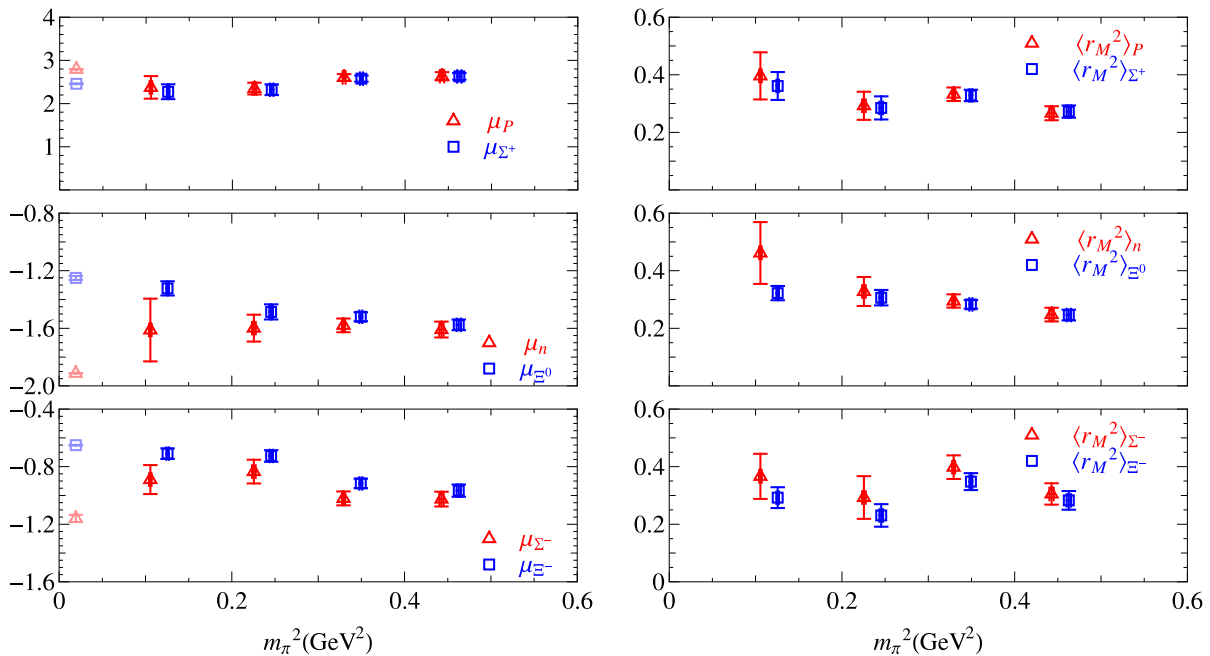


FIG. 13: Left: Baryon magnetic moments in units of  $\mu_N$  as functions of  $m_\pi^2$  (in  $\text{GeV}^2$ ). The leftmost points are the experimental numbers. Right: The magnetic mean-squared radii, in units of  $\text{fm}^2$ , as functions of  $m_\pi^2$  (in  $\text{GeV}^2$ )

From now on, we concentrate on the  $C = 1.2$  case only. Tables VI and Figure 15 summarize the fitted results when including the NNLO  $m_\pi^2$  terms. We first note that the fit is dramatically improved due to the introduction of the additional free parameter. When we include the pion masses all the way up to 700 MeV, we find that the magnetic moments for the 6 octet baryons are less than  $3\sigma$  away from experiment. However, all of the fitted  $\chi^2/\text{dof}$  are larger than one, which is still pretty poor compared with the charge-radii case. The pion masses in our calculations may still be too large to apply HBXPT. We try extrapolating only the lowest two pion masses to check systematic error due to heavy pions. We find that the magnetic moments are consistent within errorbars regardless of the number of points included. It is possibly significant that as higher masses are excluded, the extrapolated central values move toward the experimental values, except for the cascades. In the cases of  $p$ ,  $n$  and  $\Sigma^+$ , the magnetic moments are consistent with experimental ones.

SU(6) symmetry predicts the ratio  $\mu_{dp}/\mu_{up}$  should be around  $-1/2$ . Compared with what we obtain in this work, as shown in the left panel of Figure 17, the ratio agrees within  $2\sigma$  for all the pion-mass points. The heaviest two pion points have roughly the same magnitude as in the quenched calculation[13]. However, at the lightest two pion masses, they are consistent with the  $-1/2$  value. The difference could be due to sea-quark effects, which become larger as the pion mass becomes smaller. A naive linear extrapolation through all the points gives  $-0.50(10)$ , consistent with the SU(6) symmetry expectations.

We also check the sum of the magnetic moments of the proton and neutron,  $\mu_p + \mu_n$ , which should be about 1 from isospin symmetry. The right panel of Figure 17 shows our lattice calculation as a function of squared pion mass. Again, the values from different pion masses are consistent with each other within 2 standard deviations and differ from 1 by about the same amount. A naive linear extrapolation suggests the sum is  $0.78(13)$ , which is consistent with experiment but about  $2\sigma$  away from 1. This symmetry is softly broken, possibly due to finite lattice-spacing effects. Finer lattice-spacing calculations would be needed to confirm this.

#### IV. CONCLUSIONS

In this work, we study of the electromagnetic form factors of the nucleon, Sigma and cascade baryons and discuss their momentum dependence and the effects of SU(3) flavor symmetry.

We re-examine the dipole fitting form as candidate to describe the momentum dependence of these form factors. In most cases this is adequate to fit the data, however in the case of of the electric form factor  $G_E$  a new fit form motivated

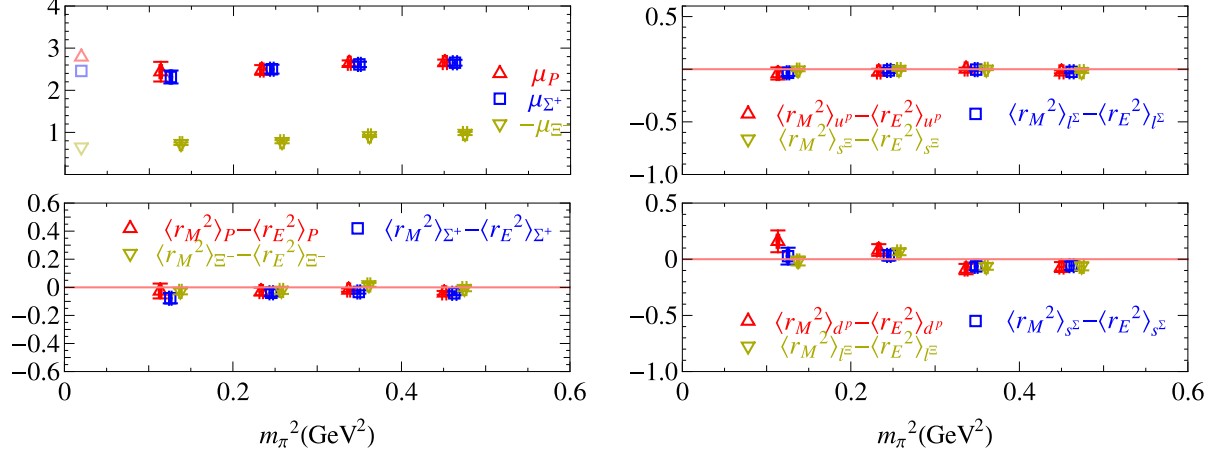


FIG. 14: Left: Magnetic moments (top, in units of  $\mu_N$ ) and the differences between magnetic and electric mean-squared radii (bottom, in units of  $\text{fm}^2$ ) as functions of  $m_\pi^2$  (in  $\text{GeV}^2$ ) for the proton,  $\Sigma^+$  and  $\Xi^-$  from fitting over  $G_M/G_E$ . Right: The differences between magnetic and electric mean-squared radii quark contributions from fitting over  $G_M/G_E$ .

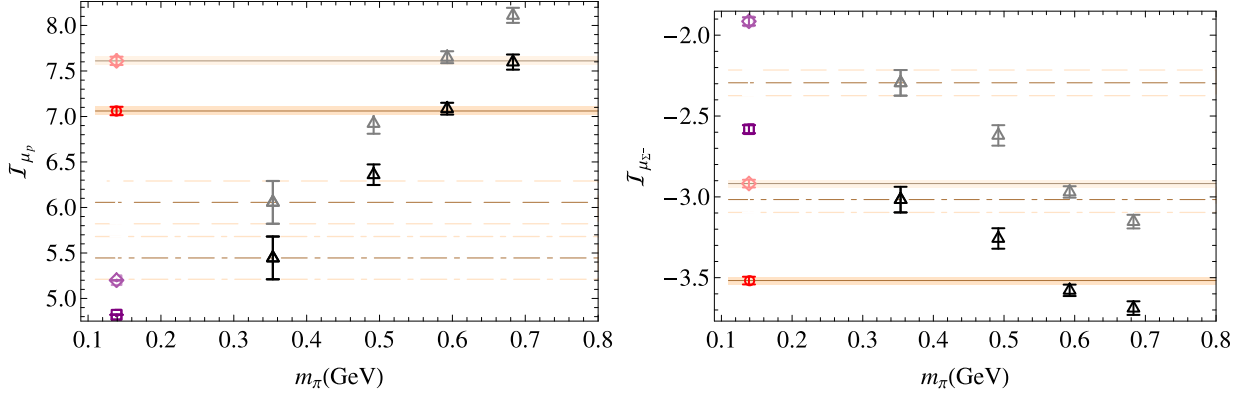


FIG. 15: Examples of  $\mathcal{T}_{\mu_B}$  as functions of pion mass. The lines and bands indicate the chiral extrapolations using Eq. 42. The symbols are as in Fig. 12.

$m_\pi^2(\text{GeV}^2)$	$p$	$n$	$\Sigma^+$	$\Sigma^-$	$\Xi^-$	$\Xi^0$
0.1256(15)	2.4(3)	-1.6(2)	2.27(17)	-0.89(10)	-0.71(4)	-1.32(5)
0.246(2)	2.35(14)	-1.60(9)	2.32(12)	-0.83(8)	-0.73(4)	-1.49(5)
0.3493(17)	2.60(8)	-1.58(5)	2.58(7)	-1.02(5)	-0.92(3)	-1.52(3)
0.463(3)	2.63(10)	-1.61(6)	2.63(8)	-1.03(5)	-0.97(4)	-1.58(4)

TABLE IV:  $\mu_B$  (in units of  $\mu_N$ ) for octet baryons from dipole-fitted magnetic form factors

$m_\pi^2(\text{GeV}^2)$	$p$	$\Sigma^+$	$n$	$\Xi^0$	$\Sigma^-$	$\Xi^-$
0.1254(15)	0.40(8)	0.36(5)	0.46(11)	0.32(2)	0.37(8)	0.29(4)
0.245(2)	0.29(5)	0.28(4)	0.33(5)	0.31(3)	0.29(7)	0.23(4)
0.3487(17)	0.33(2)	0.328(20)	0.29(2)	0.283(15)	0.40(4)	0.35(3)
0.462(2)	0.27(2)	0.27(2)	0.25(2)	0.246(19)	0.31(4)	0.28(3)

TABLE V: Mean-squared magnetic radii for octet baryons

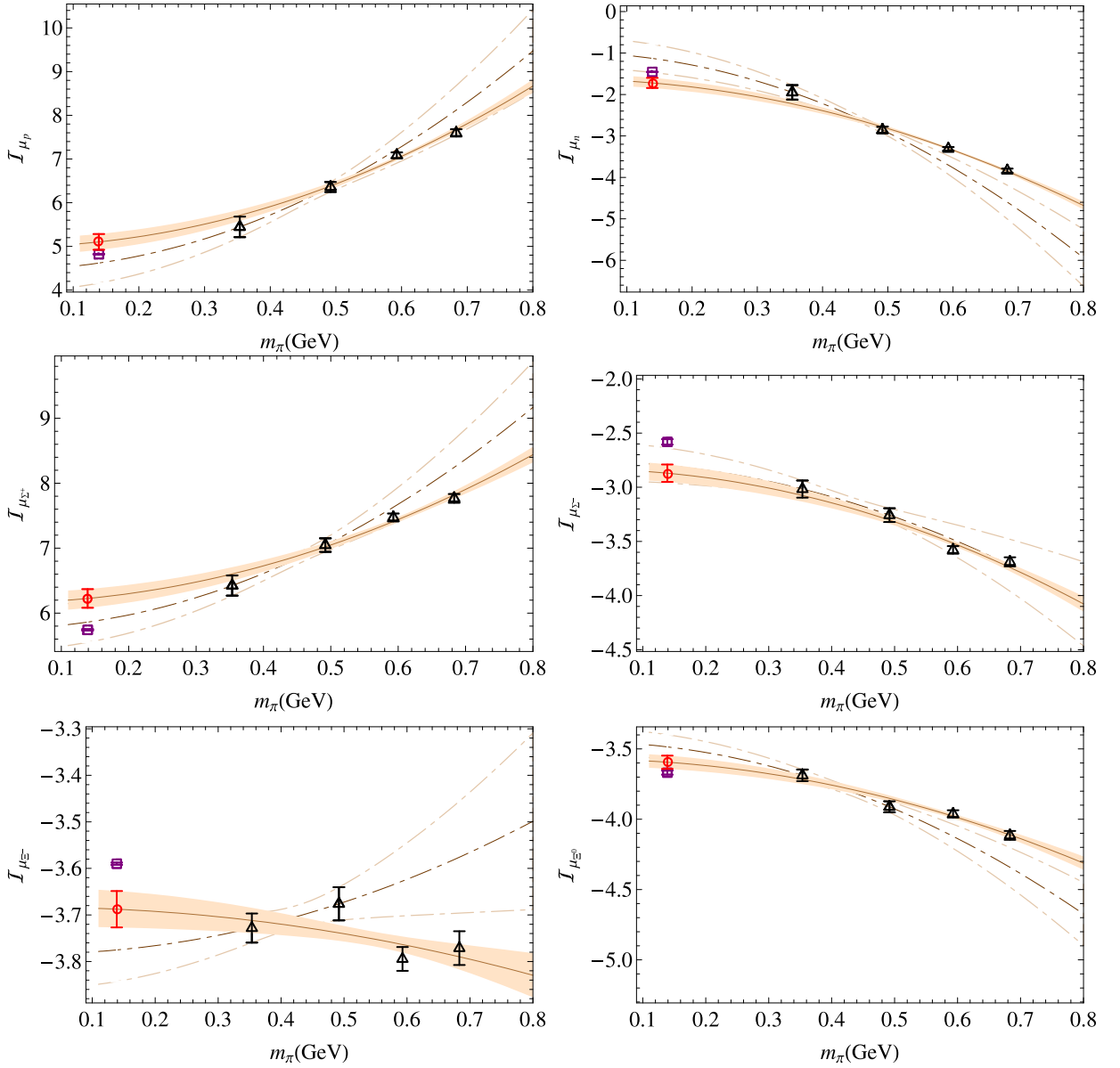


FIG. 16: Chiral extrapolations of  $\mathcal{I}_{\mu_B}$  with  $C = 1.2(2)$  according to Eq. 44. The triangles are the lattice data for  $\mathcal{I}_{\mu_B}$ , the circles are the extrapolations to the physical point, and the squares are the corresponding experimental values in terms of  $\mathcal{I}_{\mu_B}$ . The solid band is the extrapolation using all ensembles while the dot-dashed lines use the lightest two pion masses only.

by the phenomenological fit forms used by Refs. [34, 37] is introduced. This form has only one new parameter relative to the standard dipole fit.

We study the  $Q^2$  dependence of the form-factor ratios  $\mu_B G_{E,B}/G_{M,B}$  and the individual form factors  $G_{E,B}$  and  $G_{M,B}/\mu_B$ . In most cases, the pion-mass dependence is small throughout the kinematic region of this calculation. Most of the ratios are below 1, except for the  $\Xi^-$  case. The values for  $\Sigma$  and  $\Xi$  hyperons are higher than for the nucleon, and also higher than the phenomenological fits to the experimental nucleon form factor data.

The charge radii are obtained from the modified dipole fit form in Subsec. III C. SU(3) symmetry breaking in the quark sector is relatively small, and there is only mild dependence on the baryon species. Similar relations can be seen between the SU(3) partners  $p$  and  $\Sigma^+$  (or  $\Sigma^-$  and  $\Xi^-$ ). We use NLO HB $\chi$ P T to extrapolate the charge radii for the  $p$ ,  $\Sigma^+$ ,  $\Sigma^-$  and  $\Xi^-$  baryons to the physical limit. The fits work very well for all baryon flavors and are consistent regardless of whether the largest-pion mass ensembles are included. We find that including the decuplet degrees of freedom has no significant effect on the final extrapolated charge radii. The extrapolated electric mean-squared charge radii for the proton and  $\Sigma^-$  ( $0.54(7)$  and  $0.32(2)$  fm $^2$ ) are  $3.4$  and  $4.3\sigma$  away from the experimental ones. The electric

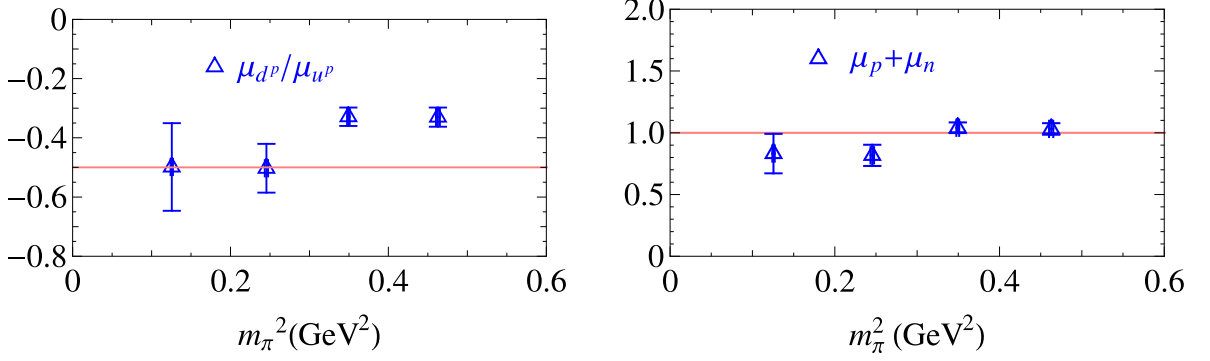


FIG. 17: Left: Magnetic moment ratios of up and down-quark contributions inside the proton. The straight line indicates the SU(6) prediction of  $-1/2$ .

Right: The sum of the magnetic moments of the proton and neutron. The line indicates 1, as predicted by isospin symmetry

$m_\pi^2(\text{GeV}^2)$	$p$	$n$	$\Sigma^+$	$\Sigma^-$	$\Xi^-$	$\Xi^0$
0.1256(15)	2.4(2)	-1.59(17)	2.27(16)	-0.88(8)	-0.71(3)	-1.32(4)
0.246(2)	2.46(11)	-1.66(8)	2.47(10)	-0.87(6)	-0.77(4)	-1.52(4)
0.3493(17)	2.61(7)	-1.59(4)	2.58(6)	-0.99(4)	-0.90(3)	-1.53(3)
0.463(3)	2.64(8)	-1.62(5)	2.63(7)	-1.02(4)	-0.97(4)	-1.59(3)
	NNLO					
$C = 1.2$	3.07(18)[1.72]	-2.18(12)[1.75]	2.94(14)[1.54]	-1.45(8)[2.85]	-0.75(4)[2.54]	-1.18(5)[1.59]
$C = 1.2$ 2pt	2.6(5)[n/a]	-1.6(3)[n/a]	2.6(3)[n/a]	-1.38(16)[n/a]	-0.84(7)[n/a]	-1.07(9)[n/a]
Exp't	2.7928474(3)	-1.9130427(5)	2.458(10)	-1.16(3)	-0.651(3)	-1.250(14)

TABLE VI:  $\mu_B$  (in units of  $\mu_N$ ) for octet baryons from fitting the ratio  $\frac{G_M}{G_E}$ . The extrapolations are done with HBXPT according to Eq. 44 with  $C = 1.2(2)$  and  $C = 0$  (if specified).

charge radii of the  $\Sigma^+$  and  $\Xi^-$  are predicted to be 0.67(5) and 0.306(15) fm<sup>2</sup> respectively.

The magnetic moments are obtained by two different approaches: traditional dipole fits to the magnetic form factors to get magnetic moments, and a linear-ansatz fit to the form factor ratio  $G_{M,B}/G_{E,B}$ . We find the extracted magnetic moments are consistent between these two methods indicating that systematic errors due to  $Q^2$  extrapolation are under control. The magnetic radii are approximately the same as the electric radii; the maximum deviation is about 10%. For the chiral extrapolation of the magnetic moments we use NLO HBXPT and find that such fits work only if we add terms with the functional form dictated by NNLO but with free coefficients. Using all ensembles, we find that the magnetic moments for the 6 octet baryons we studied are within a few standard deviations of the experimental values.

In all cases an unknown systematic error needs to be assigned due to volume, lattices spacing, and chiral extrapolations<sup>3</sup>. In addition, in all cases we have ignored the coupling of the electromagnetic current to vacuum polarization loops. This last omission may be justified on the basis of recent calculations of such disconnected diagrams for the proton form factors[54, 55]. Addressing the above systematics is the focus of future work using high statistics improved Wilson fermion calculations on anisotropic lattices[56, 57].

<sup>3</sup> Mixed-action HBXPT formulas can be obtained using PQCD results [41, 51], following the suggestion in Ref. [52]. However, given the computed value of the mixed pion mass [53], which is found to be smaller than our pion masses, such effects are expected to be sub-leading. Such behavior was also observed in the LHPC mixed-action spectroscopy calculation on these lattices [32].

### Acknowledgements

We thank the LHPC and NPLQCD collaborations for their light- and strange-quark forward and (some of the) backward propagators. We would also like to thank Brian C. Tiburzi for detailed discussions on SU(3) heavy-baryon chiral perturbation theory for charge radii and magnetic moments. These calculations were performed using the Chroma software suite[58] on clusters at Jefferson Laboratory using time awarded under the SciDAC Initiative. This work is supported by Jefferson Science Associates, LLC under U.S. DOE Contract No. DE-AC05-06OR23177. The U.S. Government retains a non-exclusive, paid-up, irrevocable, world-wide license to publish or reproduce this manuscript for U.S. Government purposes. KO is supported in part by the Jeffress Memorial Trust grant J-813, DOE OJI grant DE-FG02-07ER41527 and DOE grant DE-FG02-04ER41302.

### Appendix

In this section, we collect the details of the bare form factors for each pion-mass ensemble and momentum transfer in the Tables. Note that the magnetic form factors are naturally converted into units of  $\frac{e}{2m_B}$ , where the  $m_B$  is the baryon mass calculated in its corresponding pion sea.

$Q^2(\text{GeV}^2)$	$F_1^u$	$F_1^d$	$F_1^p$	$F_1^n$	$F_2^u$	$F_2^d$	$F_2^p$	$F_2^n$
0	1.80(6)	0.91(3)	0.90(3)	0.0074(11)	n/a	n/a	n/a	n/a
0.2358(5)	1.27(4)	0.60(2)	0.65(2)	-0.022(10)	0.73(15)	-1.04(10)	0.83(10)	-0.94(7)
0.4537(16)	0.98(5)	0.43(2)	0.51(3)	-0.040(13)	0.68(11)	-0.68(7)	0.68(7)	-0.68(5)
0.657(3)	0.77(6)	0.33(3)	0.40(4)	-0.036(18)	0.62(14)	-0.53(9)	0.59(9)	-0.56(7)
0.849(5)	0.60(8)	0.26(4)	0.32(5)	-0.03(2)	0.18(16)	-0.33(13)	0.23(11)	-0.28(9)

TABLE VII: Bare nucleon form factors as a function of  $Q^2$  at  $m_\pi = 0.354(2)$  GeV

$Q^2(\text{GeV}^2)$	$F_1^u$	$F_1^d$	$F_1^p$	$F_1^n$	$F_2^u$	$F_2^d$	$F_2^p$	$F_2^n$
0	1.807(2)	0.9159(14)	0.8997(13)	0.0081(8)	n/a	n/a	n/a	n/a
0.2379(3)	1.323(17)	0.642(9)	0.668(10)	-0.013(6)	0.84(10)	-1.16(7)	0.95(6)	-1.05(4)
0.4609(11)	1.05(3)	0.495(14)	0.535(15)	-0.020(8)	0.70(9)	-0.86(6)	0.75(5)	-0.80(4)
0.671(2)	0.90(5)	0.40(2)	0.47(3)	-0.032(12)	0.55(10)	-0.73(7)	0.61(7)	-0.67(5)
0.872(3)	0.70(5)	0.30(3)	0.37(3)	-0.035(15)	0.45(13)	-0.51(7)	0.47(8)	-0.49(5)
1.062(5)	0.68(7)	0.29(3)	0.36(4)	-0.035(15)	0.45(12)	-0.46(7)	0.45(8)	-0.45(6)

TABLE VIII: Bare nucleon form factors as a function of  $Q^2$  at  $m_\pi = 0.495(2)$  GeV

$Q^2(\text{GeV}^2)$	$F_1^u$	$F_1^d$	$F_1^p$	$F_1^n$	$F_2^u$	$F_2^d$	$F_2^p$	$F_2^n$
0	1.7884(14)	0.9057(8)	0.8903(8)	0.0077(4)	n/a	n/a	n/a	n/a
0.23874(19)	1.327(8)	0.636(4)	0.672(5)	-0.018(3)	1.00(5)	-1.07(3)	1.03(3)	-1.05(2)
0.4639(7)	1.037(12)	0.472(7)	0.534(7)	-0.031(4)	0.80(4)	-0.85(3)	0.82(3)	-0.832(19)
0.6776(14)	0.848(18)	0.367(9)	0.443(10)	-0.038(6)	0.64(5)	-0.70(3)	0.66(3)	-0.68(2)
0.881(2)	0.70(2)	0.298(11)	0.368(12)	-0.035(6)	0.43(5)	-0.55(4)	0.47(3)	-0.51(3)
1.077(3)	0.60(2)	0.239(12)	0.319(14)	-0.040(6)	0.37(4)	-0.50(4)	0.41(3)	-0.45(2)
1.264(4)	0.54(4)	0.202(18)	0.29(2)	-0.044(9)	0.33(6)	-0.48(5)	0.38(4)	-0.43(4)

TABLE IX: Bare nucleon form factors as a function of  $Q^2$  at  $m_\pi = 0.5911(15)$  GeV

$Q^2(\text{GeV}^2)$	$F_1^u$	$F_1^d$	$F_1^p$	$F_1^n$	$F_2^u$	$F_2^d$	$F_2^p$	$F_2^n$
0	1.79(3)	0.904(16)	0.889(16)	0.0072(5)	n/a	n/a	n/a	n/a
0.23991(12)	1.36(3)	0.656(13)	0.690(13)	-0.017(3)	1.16(6)	-1.10(4)	1.14(4)	-1.12(3)
0.4681(4)	1.09(2)	0.494(12)	0.559(12)	-0.032(4)	0.91(5)	-0.87(4)	0.90(3)	-0.89(3)
0.6862(9)	0.89(2)	0.384(12)	0.463(13)	-0.040(5)	0.75(5)	-0.70(4)	0.73(3)	-0.71(3)
0.8953(15)	0.77(3)	0.329(14)	0.406(16)	-0.038(6)	0.67(7)	-0.63(4)	0.66(5)	-0.64(4)
1.097(2)	0.66(3)	0.264(15)	0.354(17)	-0.045(7)	0.56(6)	-0.53(4)	0.55(4)	-0.54(3)
1.291(3)	0.57(5)	0.211(21)	0.31(2)	-0.048(8)	0.48(7)	-0.45(5)	0.47(5)	-0.46(4)

TABLE X: Bare nucleon form factors as a function of  $Q^2$  at  $m_\pi = 0.6803(18)$  GeV

$Q^2(\text{GeV}^2)$	$F_1^l$	$F_1^s$	$F_1^{\Sigma^+}$	$F_1^{\Sigma^-}$	$F_2^l$	$F_2^s$	$F_2^{\Sigma^+}$	$F_2^{\Sigma^-}$
0	1.80(4)	0.895(20)	0.902(21)	-0.898(21)	n/a	n/a	n/a	n/a
0.23857(20)	1.28(3)	0.650(17)	0.637(18)	-0.644(16)	1.14(13)	-1.01(6)	1.10(8)	-0.04(5)
0.4633(7)	0.96(3)	0.492(17)	0.478(18)	-0.485(15)	0.91(9)	-0.81(6)	0.88(6)	-0.03(4)
0.6764(15)	0.76(4)	0.389(20)	0.38(2)	-0.384(16)	0.74(11)	-0.69(6)	0.72(7)	-0.02(4)
0.879(2)	0.63(4)	0.32(2)	0.31(3)	-0.316(19)	0.54(12)	-0.46(7)	0.51(8)	-0.02(5)
1.074(3)	0.54(4)	0.26(2)	0.27(3)	-0.267(19)	0.48(9)	-0.40(7)	0.45(6)	-0.02(4)

TABLE XI: Bare Sigma form factors as a function of  $Q^2$  at  $m_\pi = 0.354(2)$  GeV

$Q^2(\text{GeV}^2)$	$F_1^l$	$F_1^s$	$F_1^{\Sigma^+}$	$F_1^{\Sigma^-}$	$F_2^l$	$F_2^s$	$F_2^{\Sigma^+}$	$F_2^{\Sigma^-}$
0	1.801(2)	0.9021(14)	0.8999(13)	-0.9010(11)	n/a	n/a	n/a	n/a
0.2392(2)	1.326(14)	0.672(7)	0.660(8)	-0.666(6)	1.09(9)	-1.17(5)	1.11(6)	0.03(4)
0.4657(8)	1.039(21)	0.530(11)	0.516(12)	-0.523(9)	0.85(8)	-0.94(5)	0.88(5)	0.03(3)
0.6812(16)	0.88(3)	0.441(17)	0.437(18)	-0.439(15)	0.65(9)	-0.80(5)	0.70(6)	0.05(4)
0.887(3)	0.71(4)	0.340(21)	0.36(2)	-0.351(17)	0.57(11)	-0.60(6)	0.58(7)	0.01(5)
1.085(4)	0.66(4)	0.31(2)	0.33(2)	-0.32(2)	0.53(10)	-0.57(7)	0.54(6)	0.01(4)
1.275(5)	0.64(7)	0.32(4)	0.32(4)	-0.32(4)	0.42(13)	-0.52(9)	0.45(9)	0.03(6)

TABLE XII: Bare Sigma form factors as a function of  $Q^2$  at  $m_\pi = 0.495(2)$  GeV

$Q^2(\text{GeV}^2)$	$F_1^l$	$F_1^s$	$F_1^{\Sigma^+}$	$F_1^{\Sigma^-}$	$F_2^l$	$F_2^s$	$F_2^{\Sigma^+}$	$F_2^{\Sigma^-}$
0	1.7853(14)	0.8953(8)	0.8917(8)	-0.8935(6)	n/a	n/a	n/a	n/a
0.23954(11)	1.322(7)	0.653(4)	0.664(4)	-0.658(3)	1.13(5)	-1.12(3)	1.12(3)	0.00(2)
0.4668(4)	1.032(11)	0.497(6)	0.522(6)	-0.510(5)	0.90(4)	-0.89(2)	0.90(3)	-0.002(18)
0.6834(8)	0.837(15)	0.391(8)	0.428(9)	-0.409(7)	0.71(4)	-0.75(3)	0.72(3)	0.011(19)
0.8909(13)	0.697(18)	0.321(10)	0.358(11)	-0.339(8)	0.51(5)	-0.59(3)	0.54(3)	0.03(2)
1.0902(19)	0.590(21)	0.261(11)	0.306(12)	-0.284(10)	0.43(4)	-0.53(3)	0.47(3)	0.030(19)
1.282(3)	0.52(3)	0.218(15)	0.272(16)	-0.245(14)	0.38(5)	-0.49(4)	0.42(3)	0.04(2)

TABLE XIII: Bare Sigma form factors as a function of  $Q^2$  at  $m_\pi = 0.5911(15)$  GeV

$Q^2(\text{GeV}^2)$	$F_1^l$	$F_1^s$	$F_1^{\Sigma^+}$	$F_1^{\Sigma^-}$	$F_2^l$	$F_2^s$	$F_2^{\Sigma^+}$	$F_2^{\Sigma^-}$
0	1.7744(16)	0.8930(9)	0.8853(9)	-0.8891(8)	n/a	n/a	n/a	n/a
0.24018(11)	1.353(8)	0.658(4)	0.683(5)	-0.670(4)	1.20(6)	-1.11(3)	1.17(4)	-0.03(2)
0.4691(4)	1.075(12)	0.502(7)	0.550(7)	-0.526(6)	0.95(5)	-0.89(3)	0.93(3)	-0.021(20)
0.6882(8)	0.876(17)	0.393(9)	0.453(9)	-0.423(8)	0.78(5)	-0.71(3)	0.76(3)	-0.02(2)
0.8987(13)	0.76(2)	0.336(11)	0.397(13)	-0.366(10)	0.68(6)	-0.64(4)	0.67(4)	-0.01(3)
1.1014(19)	0.65(3)	0.271(13)	0.343(14)	-0.307(12)	0.57(5)	-0.53(4)	0.56(4)	-0.01(2)
1.297(3)	0.55(4)	0.219(18)	0.294(20)	-0.257(17)	0.49(7)	-0.46(5)	0.48(5)	-0.01(3)

TABLE XIV: Bare Sigma form factors as a function of  $Q^2$  at  $m_\pi = 0.6803(18)$  GeV

$Q^2(\text{GeV}^2)$	$F_1^l$	$F_1^s$	$F_1^{\Xi^-}$	$F_1^{\Xi^0}$	$F_2^l$	$F_2^s$	$F_2^{\Xi^-}$	$F_2^{\Xi^0}$
0	0.914(14)	1.78(3)	-0.897(14)	0.0169(5)	n/a	n/a	n/a	n/a
0.23945(10)	0.612(11)	1.36(2)	-0.657(11)	-0.045(3)	-1.11(4)	1.01(5)	0.04(2)	-1.08(3)
0.4665(4)	0.435(10)	1.080(20)	-0.505(9)	-0.070(5)	-0.81(3)	0.78(4)	0.012(19)	-0.80(2)
0.6828(7)	0.316(10)	0.88(2)	-0.398(10)	-0.083(6)	-0.66(3)	0.62(4)	0.013(20)	-0.64(2)
0.8898(12)	0.257(13)	0.75(2)	-0.336(11)	-0.079(8)	-0.48(4)	0.53(5)	-0.02(2)	-0.50(3)
1.0886(17)	0.198(11)	0.65(2)	-0.281(11)	-0.083(7)	-0.40(3)	0.43(5)	-0.013(20)	-0.41(2)
1.280(2)	0.157(14)	0.57(3)	-0.241(14)	-0.084(9)	-0.33(3)	0.36(5)	-0.01(2)	-0.34(3)

TABLE XV: Bare cascade form factors as a function of  $Q^2$  at  $m_\pi = 0.354(2)$  GeV

$Q^2(\text{GeV}^2)$	$F_1^l$	$F_1^s$	$F_1^{\Xi^-}$	$F_1^{\Xi^0}$	$F_2^l$	$F_2^s$	$F_2^{\Xi^-}$	$F_2^{\Xi^0}$
0	0.9110(9)	1.7743(16)	-0.8951(8)	0.0159(5)	n/a	n/a	n/a	n/a
0.23978(13)	0.643(5)	1.364(8)	-0.669(4)	-0.026(3)	-1.19(4)	0.99(6)	0.07(3)	-1.13(3)
0.4676(5)	0.484(8)	1.101(14)	-0.528(7)	-0.044(4)	-0.88(3)	0.81(5)	0.02(2)	-0.86(2)
0.6852(10)	0.386(11)	0.936(21)	-0.441(10)	-0.054(6)	-0.72(4)	0.65(6)	0.02(3)	-0.70(2)
0.8937(16)	0.306(14)	0.77(3)	-0.358(12)	-0.052(8)	-0.55(5)	0.51(8)	0.01(3)	-0.54(3)
1.094(2)	0.271(16)	0.70(3)	-0.323(15)	-0.052(8)	-0.46(4)	0.46(7)	0.00(3)	-0.46(3)
1.288(3)	0.26(2)	0.67(4)	-0.31(2)	-0.051(10)	-0.43(5)	0.39(8)	0.01(3)	-0.41(4)

TABLE XVI: Bare cascade form factors as a function of  $Q^2$  at  $m_\pi = 0.495(2)$  GeV

$Q^2(\text{GeV}^2)$	$F_1^l$	$F_1^s$	$F_1^{\Xi^-}$	$F_1^{\Xi^0}$	$F_2^l$	$F_2^s$	$F_2^{\Xi^-}$	$F_2^{\Xi^0}$
0	0.9034(6)	1.7660(11)	-0.8898(5)	0.0136(3)	n/a	n/a	n/a	n/a
0.23991(8)	0.636(3)	1.348(5)	-0.662(3)	-0.0253(17)	-1.13(2)	1.06(4)	0.023(16)	-1.110(17)
0.4681(3)	0.473(5)	1.072(9)	-0.515(4)	-0.042(3)	-0.879(21)	0.86(3)	0.007(14)	-0.872(14)
0.6862(6)	0.365(7)	0.880(13)	-0.415(6)	-0.050(4)	-0.72(2)	0.69(3)	0.008(15)	-0.708(16)
0.8954(10)	0.295(8)	0.746(16)	-0.347(7)	-0.052(4)	-0.58(3)	0.51(4)	0.023(18)	-0.557(19)
1.0966(14)	0.236(9)	0.632(18)	-0.289(8)	-0.053(4)	-0.51(3)	0.43(3)	0.026(16)	-0.482(18)
1.2909(19)	0.195(11)	0.55(2)	-0.248(11)	-0.053(6)	-0.46(3)	0.36(4)	0.033(18)	-0.42(2)

TABLE XVII: Bare cascade form factors as a function of  $Q^2$  at  $m_\pi = 0.5911(15)$  GeV

$Q^2(\text{GeV}^2)$	$F_1^l$	$F_1^s$	$F_1^{\Xi^-}$	$F_1^{\Xi^0}$	$F_2^l$	$F_2^s$	$F_2^{\Xi^-}$	$F_2^{\Xi^0}$
0	0.8977(9)	1.7636(15)	-0.8871(7)	0.0106(4)	n/a	n/a	n/a	n/a
0.24035(9)	0.651(4)	1.363(7)	-0.671(3)	-0.021(2)	-1.12(3)	1.16(5)	-0.01(2)	-1.14(2)
0.4697(3)	0.491(6)	1.094(11)	-0.528(5)	-0.037(3)	-0.89(3)	0.93(4)	-0.013(19)	-0.899(20)
0.6895(7)	0.380(9)	0.898(15)	-0.426(7)	-0.046(4)	-0.71(3)	0.76(4)	-0.019(20)	-0.73(2)
0.9007(11)	0.321(10)	0.787(21)	-0.369(10)	-0.048(6)	-0.63(4)	0.67(6)	-0.01(2)	-0.64(3)
1.1044(16)	0.257(12)	0.67(2)	-0.310(11)	-0.052(6)	-0.53(4)	0.56(5)	-0.01(2)	-0.54(3)
1.301(2)	0.204(15)	0.57(3)	-0.259(16)	-0.055(7)	-0.45(4)	0.49(6)	-0.02(3)	-0.46(4)

TABLE XVIII: Bare cascade form factors as a function of  $Q^2$  at  $m_\pi = 0.6803(18)$  GeV

$Q^2(\text{GeV}^2)$	$G_E^u$	$G_E^d$	$G_E^p$	$G_M^u$	$G_M^d$	$G_M^p$	$G_M^n$
0	1.80(6)	0.91(3)	0.90(3)	n/a	n/a	n/a	n/a
0.2358(5)	1.30(5)	0.555(21)	0.61(2)	2.00(16)	-0.44(10)	1.48(11)	-0.96(8)
0.4537(16)	1.03(5)	0.37(2)	0.45(2)	1.66(14)	-0.26(7)	1.19(9)	-0.72(6)
0.657(3)	0.84(7)	0.26(3)	0.33(3)	1.39(18)	-0.20(9)	0.99(11)	-0.60(7)
0.849(5)	0.63(9)	0.20(4)	0.28(4)	0.78(20)	n/a	0.55(13)	-0.31(10)

TABLE XIX: Bare nucleon form factors as a function of  $Q^2$  at  $m_\pi = 0.354(2)$  GeV

$Q^2(\text{GeV}^2)$	$G_E^u$	$G_E^d$	$G_E^p$	$G_M^u$	$G_M^d$	$G_M^p$	$G_M^n$
0	1.807(2)	0.9159(14)	0.8997(13)	n/a	n/a	n/a	n/a
0.2379(3)	1.353(18)	0.600(10)	0.634(10)	2.16(10)	-0.52(7)	1.62(6)	-1.07(4)
0.4609(11)	1.10(3)	0.436(14)	0.483(14)	1.75(10)	-0.36(6)	1.29(6)	-0.82(4)
0.671(2)	0.96(5)	0.33(2)	0.41(2)	1.46(13)	-0.33(7)	1.08(8)	-0.70(5)
0.872(3)	0.76(6)	0.23(3)	0.31(3)	1.15(15)	-0.21(7)	0.83(10)	-0.52(6)
1.062(5)	0.75(8)	0.21(3)	0.28(3)	1.13(16)	-0.17(7)	0.81(11)	-0.49(7)

TABLE XX: Bare nucleon form factors as a function of  $Q^2$  at  $m_\pi = 0.495(2)$  GeV

$Q^2(\text{GeV}^2)$	$G_E^u$	$G_E^d$	$G_E^p$	$G_M^u$	$G_M^d$	$G_M^p$	$G_M^n$
0	1.7884(14)	0.9057(8)	0.8903(8)	n/a	n/a	n/a	n/a
0.23874(19)	1.359(9)	0.602(4)	0.639(4)	2.33(5)	-0.44(3)	1.70(3)	-1.07(2)
0.4639(7)	1.087(13)	0.420(7)	0.483(6)	1.84(5)	-0.37(3)	1.35(3)	-0.863(21)
0.6776(14)	0.906(19)	0.303(9)	0.383(9)	1.48(5)	-0.34(3)	1.10(4)	-0.72(2)
0.881(2)	0.75(2)	0.233(11)	0.312(11)	1.14(6)	-0.25(4)	0.84(4)	-0.55(3)
1.077(3)	0.65(3)	0.167(12)	0.259(12)	0.97(6)	-0.26(3)	0.73(4)	-0.49(3)
1.264(4)	0.59(5)	0.122(17)	0.225(18)	0.86(8)	-0.27(5)	0.67(6)	-0.47(4)

TABLE XXI: Bare nucleon form factors as a function of  $Q^2$  at  $m_\pi = 0.5911(15)$  GeV

$Q^2(\text{GeV}^2)$	$G_E^u$	$G_E^d$	$G_E^p$	$G_M^u$	$G_M^d$	$G_M^p$	$G_M^n$
0	1.79(3)	0.904(16)	0.889(16)	n/a	n/a	n/a	n/a
0.23991(12)	1.39(3)	0.626(12)	0.659(13)	2.52(7)	-0.45(3)	1.83(5)	-1.14(3)
0.4681(4)	1.13(2)	0.448(11)	0.512(12)	2.00(6)	-0.38(3)	1.46(4)	-0.92(3)
0.6862(9)	0.94(3)	0.330(12)	0.407(12)	1.63(6)	-0.31(3)	1.19(4)	-0.75(3)
0.8953(15)	0.84(3)	0.266(13)	0.339(13)	1.45(9)	-0.30(4)	1.06(6)	-0.68(4)
1.097(2)	0.73(4)	0.199(13)	0.287(14)	1.22(8)	-0.26(4)	0.90(5)	-0.58(4)
1.291(3)	0.63(5)	0.145(18)	0.239(20)	1.04(11)	-0.24(5)	0.78(7)	-0.51(5)

TABLE XXII: Bare nucleon form factors as a function of  $Q^2$  at  $m_\pi = 0.6803(18)$  GeV

$Q^2(\text{GeV}^2)$	$G_E^l$	$G_E^s$	$G_E^{\Sigma^+}$	$G_E^{\Sigma^-}$	$G_M^l$	$G_M^s$	$G_M^{\Sigma^+}$	$G_M^{\Sigma^-}$
0	1.80(4)	0.895(20)	0.902(21)	-0.898(21)	n/a	n/a	n/a	n/a
0.23857(20)	1.24(3)	0.683(18)	0.601(17)	-0.642(16)	2.42(14)	-0.36(6)	1.73(9)	-0.69(5)
0.4633(7)	0.91(3)	0.544(18)	0.422(16)	-0.483(15)	1.87(11)	-0.31(5)	1.35(7)	-0.52(4)
0.6764(15)	0.70(3)	0.45(2)	0.313(20)	-0.383(16)	1.50(12)	-0.30(6)	1.10(8)	-0.40(5)
0.879(2)	0.56(4)	0.38(3)	0.25(2)	-0.313(19)	1.16(14)	-0.14(7)	0.82(10)	-0.34(6)
1.074(3)	0.47(4)	0.32(3)	0.20(2)	-0.263(19)	1.01(12)	-0.14(7)	0.72(8)	-0.29(5)

TABLE XXIII: Bare Sigma form factors as a function of  $Q^2$  at  $m_\pi = 0.354(2)$  GeV

$Q^2(\text{GeV}^2)$	$G_E^l$	$G_E^s$	$G_E^{\Sigma^+}$	$G_E^{\Sigma^-}$	$G_M^l$	$G_M^s$	$G_M^{\Sigma^+}$	$G_M^{\Sigma^-}$
0	1.801(2)	0.9021(14)	0.8999(13)	-0.9010(11)	n/a	n/a	n/a	n/a
0.2392(2)	1.293(14)	0.707(7)	0.626(8)	-0.667(6)	2.41(10)	-0.50(5)	1.77(6)	-0.64(4)
0.4657(8)	0.989(20)	0.585(12)	0.465(11)	-0.525(9)	1.89(9)	-0.41(5)	1.39(5)	-0.49(4)
0.6812(16)	0.82(3)	0.510(19)	0.378(17)	-0.444(15)	1.53(10)	-0.36(5)	1.14(7)	-0.39(4)
0.887(3)	0.65(4)	0.41(2)	0.298(21)	-0.352(18)	1.29(13)	-0.26(6)	0.94(8)	-0.34(5)
1.085(4)	0.58(4)	0.39(3)	0.26(2)	-0.32(2)	1.18(12)	-0.25(6)	0.87(8)	-0.31(5)
1.275(5)	0.58(6)	0.40(5)	0.25(3)	-0.33(4)	1.06(19)	-0.21(8)	0.78(12)	-0.29(7)

TABLE XXIV: Bare Sigma form factors as a function of  $Q^2$  at  $m_\pi = 0.495(2)$  GeV

$Q^2(\text{GeV}^2)$	$G_E^l$	$G_E^s$	$G_E^{\Sigma^+}$	$G_E^{\Sigma^-}$	$G_M^l$	$G_M^s$	$G_M^{\Sigma^+}$	$G_M^{\Sigma^-}$
0	1.7853(14)	0.8953(8)	0.8917(8)	-0.8935(6)	n/a	n/a	n/a	n/a
0.23954(11)	1.290(7)	0.684(4)	0.632(4)	-0.658(3)	2.45(5)	-0.46(3)	1.79(3)	-0.66(2)
0.4668(4)	0.982(10)	0.546(6)	0.472(6)	-0.509(5)	1.93(5)	-0.40(2)	1.42(3)	-0.512(19)
0.6834(8)	0.779(15)	0.451(9)	0.369(8)	-0.410(7)	1.55(5)	-0.36(3)	1.15(3)	-0.399(21)
0.8909(13)	0.643(17)	0.384(11)	0.300(10)	-0.342(8)	1.21(6)	-0.27(3)	0.90(4)	-0.31(2)
1.0902(19)	0.533(19)	0.329(13)	0.246(10)	-0.287(10)	1.02(5)	-0.27(3)	0.77(3)	-0.25(2)
1.282(3)	0.46(3)	0.294(18)	0.208(14)	-0.251(14)	0.90(7)	-0.28(4)	0.69(4)	-0.21(3)

TABLE XXV: Bare Sigma form factors as a function of  $Q^2$  at  $m_\pi = 0.5911(15)$  GeV

$Q^2(\text{GeV}^2)$	$G_E^l$	$G_E^s$	$G_E^{\Sigma^+}$	$G_E^{\Sigma^-}$	$G_M^l$	$G_M^s$	$G_M^{\Sigma^+}$	$G_M^{\Sigma^-}$
0	1.7744(16)	0.8930(9)	0.8853(9)	-0.8891(8)	n/a	n/a	n/a	n/a
0.24018(11)	1.322(8)	0.687(4)	0.652(4)	-0.669(4)	2.56(6)	-0.45(3)	1.86(4)	-0.70(2)
0.4691(4)	1.027(12)	0.546(7)	0.503(7)	-0.525(6)	2.02(5)	-0.38(3)	1.48(3)	-0.55(2)
0.6882(8)	0.818(16)	0.446(10)	0.397(8)	-0.421(8)	1.66(6)	-0.32(3)	1.21(4)	-0.45(2)
0.8987(13)	0.697(20)	0.397(13)	0.332(11)	-0.365(10)	1.44(8)	-0.30(4)	1.06(5)	-0.38(3)
1.1014(19)	0.58(2)	0.334(15)	0.277(12)	-0.305(12)	1.22(7)	-0.26(4)	0.90(5)	-0.32(3)
1.297(3)	0.48(3)	0.28(2)	0.227(16)	-0.255(17)	1.04(9)	-0.24(4)	0.77(6)	-0.27(3)

TABLE XXVI: Bare Sigma form factors as a function of  $Q^2$  at  $m_\pi = 0.6803(18)$  GeV

$Q^2(\text{GeV}^2)$	$G_E^l$	$G_E^s$	$G_E^{\Xi^-}$	$G_E^{\Xi^0}$	$G_M^l$	$G_M^s$	$G_M^{\Xi^-}$	$G_M^{\Xi^0}$
0	0.914(14)	1.78(3)	-0.897(14)	0.0169(5)	n/a	n/a	n/a	n/a
0.23945(10)	0.644(11)	1.33(2)	-0.658(11)	-0.014(3)	-0.50(4)	2.36(6)	-0.62(2)	-1.12(3)
0.4665(4)	0.481(10)	1.036(19)	-0.505(9)	-0.025(4)	-0.38(3)	1.86(5)	-0.49(2)	-0.87(2)
0.6828(7)	0.370(11)	0.828(20)	-0.399(10)	-0.029(6)	-0.34(3)	1.50(5)	-0.39(2)	-0.72(3)
0.8898(12)	0.309(14)	0.69(2)	-0.334(11)	-0.025(7)	-0.23(4)	1.28(7)	-0.35(3)	-0.58(3)
1.0886(17)	0.250(13)	0.59(2)	-0.280(11)	-0.030(7)	-0.20(3)	1.08(6)	-0.29(2)	-0.49(3)
1.280(2)	0.208(16)	0.51(3)	-0.240(14)	-0.031(8)	-0.17(4)	0.93(7)	-0.25(3)	-0.42(3)

TABLE XXVII: Bare cascade form factors as a function of  $Q^2$  at  $m_\pi = 0.354(2)$  GeV

$Q^2(\text{GeV}^2)$	$G_E^l$	$G_E^s$	$G_E^{\Xi^-}$	$G_E^{\Xi^0}$	$G_M^l$	$G_M^s$	$G_M^{\Xi^-}$	$G_M^{\Xi^0}$
0	0.9110(9)	1.7743(16)	-0.8951(8)	0.0159(5)	n/a	n/a	n/a	n/a
0.23978(13)	0.675(5)	1.336(8)	-0.671(4)	0.005(3)	-0.55(4)	2.36(6)	-0.60(3)	-1.15(3)
0.4676(5)	0.532(8)	1.057(14)	-0.530(7)	0.002(4)	-0.40(3)	1.91(6)	-0.50(2)	-0.90(2)
0.6852(10)	0.443(12)	0.884(20)	-0.443(10)	0.001(6)	-0.34(4)	1.59(6)	-0.42(3)	-0.75(3)
0.8937(16)	0.363(15)	0.72(3)	-0.360(13)	0.003(8)	-0.24(5)	1.28(9)	-0.34(4)	-0.59(3)
1.094(2)	0.329(18)	0.64(3)	-0.323(15)	0.006(8)	-0.19(4)	1.16(8)	-0.32(3)	-0.52(3)
1.288(3)	0.32(3)	0.61(4)	-0.31(2)	0.010(10)	-0.17(5)	1.06(10)	-0.30(4)	-0.47(4)

TABLE XXVIII: Bare cascade form factors as a function of  $Q^2$  at  $m_\pi = 0.495(2)$  GeV

$Q^2(\text{GeV}^2)$	$G_E^l$	$G_E^s$	$G_E^{\Xi^-}$	$G_E^{\Xi^0}$	$G_M^l$	$G_M^s$	$G_M^{\Xi^-}$	$G_M^{\Xi^0}$
0	0.9034(6)	1.7660(11)	-0.8898(5)	0.0136(3)	n/a	n/a	n/a	n/a
0.23991(8)	0.667(3)	1.320(5)	-0.662(3)	0.0047(17)	-0.50(2)	2.41(4)	-0.639(17)	-1.135(17)
0.4681(3)	0.519(5)	1.027(8)	-0.515(4)	0.003(3)	-0.406(21)	1.93(3)	-0.508(15)	-0.914(15)
0.6862(6)	0.420(7)	0.826(12)	-0.415(6)	0.004(4)	-0.35(2)	1.57(4)	-0.407(16)	-0.758(17)
0.8954(10)	0.353(9)	0.694(15)	-0.349(7)	0.004(4)	-0.29(3)	1.26(5)	-0.324(20)	-0.609(21)
1.0966(14)	0.299(10)	0.579(17)	-0.292(8)	0.006(4)	-0.27(2)	1.06(4)	-0.263(18)	-0.535(20)
1.2909(19)	0.261(13)	0.50(2)	-0.252(11)	0.009(5)	-0.26(3)	0.91(5)	-0.21(2)	-0.48(2)

TABLE XXIX: Bare cascade form factors as a function of  $Q^2$  at  $m_\pi = 0.5911(15)$  GeV

$Q^2(\text{GeV}^2)$	$G_E^l$	$G_E^s$	$G_E^{\Xi^-}$	$G_E^{\Xi^0}$	$G_M^l$	$G_M^s$	$G_M^{\Xi^-}$	$G_M^{\Xi^0}$
0	0.8977(9)	1.7636(15)	-0.8871(7)	0.0106(4)	n/a	n/a	n/a	n/a
0.24035(9)	0.679(4)	1.334(7)	-0.671(3)	0.0080(20)	-0.47(3)	2.52(5)	-0.68(2)	-1.16(2)
0.4697(3)	0.534(7)	1.048(11)	-0.528(6)	0.007(3)	-0.40(3)	2.02(5)	-0.541(20)	-0.937(21)
0.6895(7)	0.431(9)	0.843(15)	-0.425(7)	0.007(4)	-0.33(3)	1.66(5)	-0.45(2)	-0.77(2)
0.9007(11)	0.380(12)	0.724(19)	-0.368(10)	0.012(5)	-0.31(4)	1.46(7)	-0.38(3)	-0.69(3)
1.1044(16)	0.318(14)	0.61(2)	-0.308(11)	0.010(6)	-0.27(3)	1.24(6)	-0.32(2)	-0.59(3)
1.301(2)	0.265(19)	0.51(3)	-0.257(16)	0.008(7)	-0.24(4)	1.07(8)	-0.27(3)	-0.52(4)

TABLE XXX: Bare cascade form factors as a function of  $Q^2$  at  $m_\pi = 0.6803(18)$  GeV

- 
- [1] K. F. Liu, S. J. Dong, T. Draper, and W. Wilcox, Phys. Rev. Lett. **74**, 2172 (1995), hep-lat/9406007.
- [2] M. Gockeler et al. (QCDSF), Phys. Rev. **D71**, 034508 (2005), hep-lat/0303019.
- [3] C. Alexandrou, G. Koutsou, J. W. Negele, and A. Tsapalis, Phys. Rev. **D74**, 034508 (2006), hep-lat/0605017.
- [4] K. Orginos, PoS **LAT2006**, 018 (2006).
- [5] P. Hagler et al. (LHPC), Phys. Rev. **D77**, 094502 (2008), 0705.4295.
- [6] C. Alexandrou, G. Koutsou, T. Leontiou, J. W. Negele, and A. Tsapalis (2007), arXiv:0706.3011 [hep-lat].
- [7] M. Gockeler et al. (QCDSF/UKQCD), PoS **LAT2007**, 161 (2007), arXiv:0710.2159 [hep-lat].
- [8] P. Hagler, PoS **LAT2007**, 013 (2007), arXiv:0711.0819[hep-lat].
- [9] S. Sasaki and T. Yamazaki, Phys. Rev. **D78**, 014510 (2008), 0709.3150.
- [10] H.-W. Lin, T. Blum, S. Ohta, S. Sasaki, and T. Yamazaki, Phys. Rev. **D78**, 014505 (2006), arXiv:0802.0863 [hep-lat].
- [11] J. M. Zanotti, PoS **LAT2008**, 007 (2008), arXiv:0812.3845[hep-lat].
- [12] P. Wang, D. B. Leinweber, A. W. Thomas, and R. D. Young (2008), arXiv:810.1021 [hep-ph].
- [13] S. Boinpapalli, D. B. Leinweber, A. G. Williams, J. M. Zanotti, and J. B. Zhang, Phys. Rev. **D74**, 093005 (2006), hep-lat/0604022.
- [14] D. B. Leinweber, R. M. Woloshyn, and T. Draper, Phys. Rev. **D43**, 1659 (1991).
- [15] M. Gockeler et al. (QCDSF), Phys. Lett. **B545**, 112 (2002), hep-lat/0208017.
- [16] H.-W. Lin and K. Orginos (2007), arXiv:0712.1214 [hep-lat].
- [17] W. M. Yao et al. (Particle Data Group), J. Phys. **G33**, 1 (2006).
- [18] M. Gell-Mann, Phys. Rev. **125**, 1067 (1962).
- [19] S. Okubo, Prog. Theor. Phys. **27**, 949 (1962).
- [20] S. R. Beane, K. Orginos, and M. J. Savage, Phys. Lett. **B654**, 20 (2007), hep-lat/0604013.
- [21] S. R. Coleman and S. L. Glashow, Phys. Rev. Lett. **6**, 423 (1961).
- [22] H.-W. Lin (2008), arXiv:0812.0411[hep-lat].
- [23] J. Kogut and L. Susskind, Phys. Rev. **D11**, 395 (1975).
- [24] K. Orginos and D. Toussaint (MILC), Phys. Rev. **D59**, 014501 (1999), hep-lat/9805009.
- [25] K. Orginos, D. Toussaint, and R. L. Sugar (MILC), Phys. Rev. **D60**, 054503 (1999), hep-lat/9903032.
- [26] C. W. Bernard et al., Phys. Rev. **D64**, 054506 (2001), hep-lat/0104002.
- [27] D. B. Kaplan, Phys. Lett. **B288**, 342 (1992), hep-lat/9206013.
- [28] D. B. Kaplan, Nucl. Phys. Proc. Suppl. **30**, 597 (1993).
- [29] Y. Shamir, Nucl. Phys. **B406**, 90 (1993), hep-lat/9303005.
- [30] V. Furman and Y. Shamir, Nucl. Phys. **B439**, 54 (1995), hep-lat/9405004.
- [31] A. Hasenfratz and F. Knechtli, Phys. Rev. **D64**, 034504 (2001), hep-lat/0103029.
- [32] A. Walker-Loud et al. (2008), 0806.4549.
- [33] S. Durr and C. Hoelbling, Phys. Rev. **D71**, 054501 (2005), hep-lat/0411022.
- [34] J. Arrington, W. Melnitchouk, and J. A. Tjon, Phys. Rev. **C76**, 035205 (2007), 0707.1861.
- [35] C. F. Perdrisat, V. Punjabi, and M. Vanderhaeghen, Prog. Part. Nucl. Phys. **59**, 694 (2007), hep-ph/0612014.
- [36] J. Arrington, C. D. Roberts, and J. M. Zanotti, J. Phys. **G34**, S23 (2007), nucl-th/0611050.
- [37] J. J. Kelly, Phys. Rev. **C70**, 068202 (2004).
- [38] E. E. Jenkins and A. V. Manohar, Phys. Lett. **B255**, 558 (1991).
- [39] E. E. Jenkins, Nucl. Phys. **B368**, 190 (1992).
- [40] B. Kubis, T. R. Hemmert, and U.-G. Meissner, Phys. Lett. **B456**, 240 (1999), hep-ph/9903285.
- [41] D. Arndt and B. C. Tiburzi, Phys. Rev. **D68**, 094501 (2003), hep-lat/0307003.
- [42] B. Kubis and U. G. Meissner, Eur. Phys. J. **C18**, 747 (2001), hep-ph/0010283.
- [43] C. Alexandrou, G. Koutsou, T. Leontiou, J. W. Negele, and A. Tsapalis, Phys. Rev. **D76**, 094511 (2007).
- [44] S. R. Beane, P. F. Bedaque, K. Orginos, and M. J. Savage, Phys. Rev. **D75**, 094501 (2007), hep-lat/0606023.
- [45] R. G. Edwards et al. (2006), hep-lat/0610007.
- [46] T. Yamazaki and S. Ohta (RBC and UKQCD), PoS **LAT2007**, 165 (2007), arXiv:0710.0422 [hep-lat].
- [47] E. E. Jenkins, M. E. Luke, A. V. Manohar, and M. J. Savage, Phys. Lett. **B302**, 482 (1993), hep-ph/9212226.
- [48] J.-W. Chen and M. J. Savage, Phys. Rev. **D65**, 094001 (2002), hep-lat/0111050.
- [49] B. C. Tiburzi, Phys. Rev. **D72**, 094501 (2005), hep-lat/0508019.
- [50] B. C. Tiburzi, Private communication (2008).
- [51] B. C. Tiburzi, Phys. Rev. **D71**, 054504 (2005), hep-lat/0412025.
- [52] J.-W. Chen, D. O'Connell, and A. Walker-Loud (2007), arXiv:0706.0035 [hep-lat].
- [53] K. Orginos and A. Walker-Loud, Phys. Rev. **D77**, 094505 (2008), 0705.0572.
- [54] R. Babich et al., PoS **LAT2007**, 139 (2007), arXiv:0710.5536[hep-lat].
- [55] R. Lewis, W. Wilcox, and R. M. Woloshyn, Phys. Rev. **D67**, 013003 (2003), hep-ph/0210064.
- [56] R. G. Edwards, B. Joo, and H.-W. Lin, Phys. Rev. **D78**, 054501 (2008), arXiv:0803.3960[hep-lat].
- [57] H.-W. Lin et al. (2008), arXiv:0810.3588[hep-lat].
- [58] R. G. Edwards and B. Joo (SciDAC), Nucl. Phys. Proc. Suppl. **140**, 832 (2005), hep-lat/0409003.